Supporting Information

Experimental details

725 °C (24 h) --> 700 °C (48 h) --> 675 °C (24 h) --> 650 °C (24 h) --> 625 °C (48 h) --> 600 °C (24 h) --> 575 °C (24 h) --> 550 °C (48 h) --> 525 °C (24 h) --> 500 °C (24 h) --> 475 °C (24 h) --> 450 °C (24 h) --> 425 °C (24h) --> 400 °C (24h) --> Room temperature. The cooling rate in between the annealing steps were set to 0.5 °C/min.

Supporting Table 1 Cooling procedure of MO-samples (cooled over the course of ~18 days by stepwise annealing and cooling in O_2-flow).

Campaign	Campaign specific information		Beam current	Wavelength	Data points (optimized)
	Long Q-range	Optimized Q-range			
1	t = 10 s Δ2θ = 0.010 °	-	16 mA	0.6390 Å	4607
2	t = 10 s Δ2θ = 0.013°	t = 30 s Δ2θ = 0.005 °	200 mA	0.6223 Å	3611 (4856)
3			200 mA	0.6888 Å	3992 (4546)
Details on refined corrections: Most instrumental corrections were set based on measurements of a standard as mentioned in the paper. In addition some samples required further refinement, as described by th2_offset = zero_shift + (cos_shift · Cos(Th) + sin_shift · Sin(Th)), where the cos_shift parameter was refined for the individual samples to account for small changes in the sample position. These parameters were however also locked before the final refinement in most cases. Background parameters were determined by a Chebyshev polynomial with 7 parameters, and for the Long Q-range three additional (very broad) background peaks were added (around Q = 1.50, 4.75 and 6.75 Å^2), where intensity, position and width were refined (very constrained to keep it broad). That means 7+3·3 = 16 refined parameters for Campaign 1 (only Long Q-range) and an additional 7 to make it 23 refined parameters for Campaign 2 and 3 (both long and optimized Q-range).					

Supporting Table 2: Details of Powder X-ray diffraction experiments in three different campaigns at ESRF, Grenoble with additional specifications related to the refined parameters not covered in Supporting Table 3.

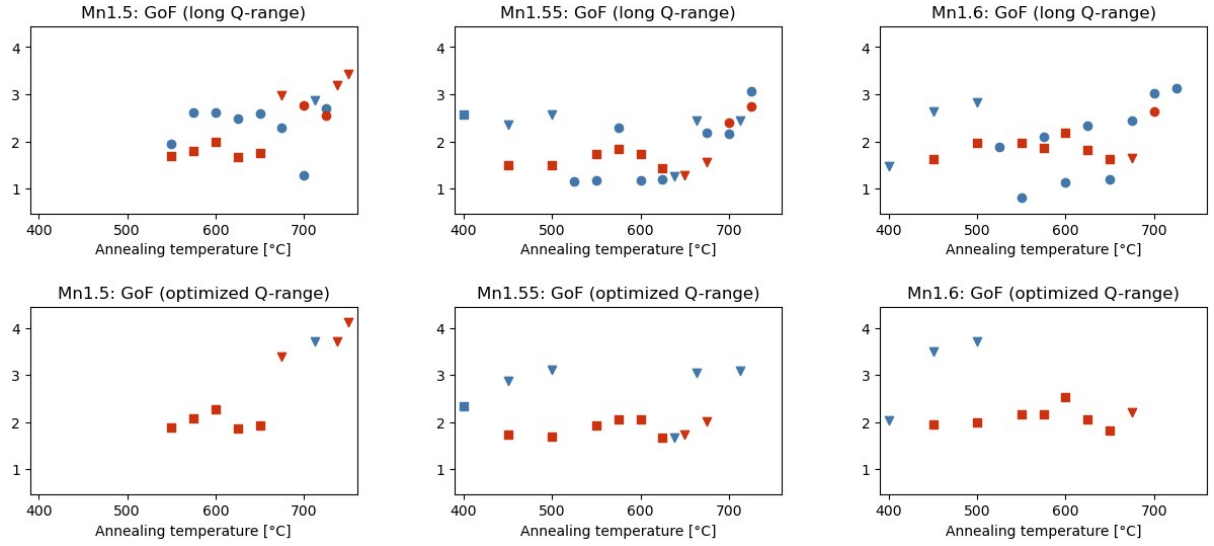

Supporting Figure 1 Showing the Goodness of Fit (GoF) as means of the quality of Rietveld refinements of samples annealed for 6 h at different temperatures in air (blue) or O_2-flow (red). The figure is also serving as an overview of which samples were measured under what campaign (see Supporting Table 2). Circles ("o") are used for measurements from Campaign 1, triangles ("Δ") for Campaign 2 and squares ("□") for Campaign 3.

Phase name	Space group	Atom	Wycoff site	x	y	z	Beq [Å^2]	Occ.	Bragg peaks
o-LMNO	P4332	Li	8c**	**x8c**	x8c	x8c	0.85	1	184 (82)
		Mn1	12d	1/8	y12d	1/4 + y12d	0.25	1	
		Ni1	12d					0	
		Ni2	4a	5/8	5/8	5/8	0.4	1	
		Mn2	4a					0	
		O1	8c	**xO1**	xO1	xO1	0.25	1	
		O2	24e	**xO2**	**yO2**	**zO2**	0.3	1	
	Variables	**a, wp%, Xi_AP, Xi_subcell, Strain_G, Strain_L**					→ 11 params		
(d/e)-LMNO	Fd-3m	Li	8a	3/8	3/8	3/8	0.8	**1***	50 (23)
		Mn1	8a				0.3	**0**	
		Ni1	8a				0.3	0	
		Mn2	16d	0	0	0	0.3	**0.75**	
		Ni2	16d				0.3	**0.25***	
		O	32e	**xO**	xO	xO	0.3	1	
	Variables	**a, wp%, CS_L, CS_G, Strain_G**					→ 10 params		
o-RS	Fm-3m	Ni1	24d	0	1/4	1/4	0.3	**1***	59 (27)
		Mn1	24d	0	1/4	1/4	0.3	0	
		Li1	24d	0	1/4	1/4	0.8	**0**	
		Mn2	4a	0	0	0	0.3	1	
		Li3	4b	1/2	1/2	1/2	0.8	**0***	
		O1	8c	1/4	1/4	1/4	0.3	1	
		O2	24e	**xO2**	0	0	0.3	1	
	Variables	**a, wp%, CS_L, CS_G, Strain_G**					→ 9 params		
Layered	R-3m	Li1	3a	0	0	0	0.8	**0**	52(18)
		Ni1	3a	0	0	0	0.3	**0.6***	
		Mn1	3a	0	0	0	0.3	0.4	
		Li2	3b	0	0	1/2	0.8	**1***	
		Ni2	3b	0	0	1/2	0.3	**0**	
		O	6c	0	0	**zO1**	0.3	1	
	Variables	**a, c, wp%, CS_L, CS_G, Strain_G**					→ 11 params		

Supporting Table 3 Details on the involved crystallographic phases, including space group and atomic positions. Refined parameters/variables are written in bold, and summarized for each phase in the table. This includes scale factor/weight percent, lattice parameters (a,c), crystallite size variable and strain components. For the o-LMNO the crystallite size estimate of the superstructure peaks (Xi_AP) are handled separately from the rest (Xi_subcell), and is only considering the Lorentzian contribution to the peak width. For o-LMNO a Lorentzian strain component is furthermore added, in addition to the gaussian strain component which all phases are refined with. All thermal parameters were fixed throughout all refinements with values written. For o-LMNO b_{eq}-values were based on Rietveld refinement of a combined ND/SXRD-data set in another work on a very ordered samples (NB: This paper is not yet published, but from the same authors). Similar values were also fixed for the other phases. For occupancies the starting values before the refinement are stated, and an asterix is put where the parameter is constrained based on other atoms in the same (or based on amount of Li in 24d-site for the case of Li in 4b-site of o-RS) to keep the site fully occupied. The number of Bragg reflexes used in the refinement, for both the long Q-range setup and the optimized detector position (parenthesis).

Rietveld Refinement details

Rock salt (o-RS) refinement:

Simulated diffraction patterns for some different site filling schemes are shown in the left panel of Supporting Figure 2, and are used as a basis when describing the restrictions included in the refinement of this phase:

- **4a-site:** Owing to low Mn/Ni-scattering contrast, we do not refine the occupancy of this site and assume this site filled with Mn. A good indicator for clarifying any mixed Mn/Ni occupancy would be the x-coordinate for oxygen in 24e (x,0,0) – i.e. the (Mn,Ni)-O bond lengths. However, changing from x = 0.25 (as in *disordered* NiO) to x = 0.231 (as in *ordered* $MnNi_6O_8$, indicated by an asterix in Supporting Figure 2 does not change diffraction pattern much.
- **24d-site:** To estimate the amount of Li in the 24d-site, Ni and Li occupancies are refined. As seen in Supporting Figure 2 there is a small intensity decrease of all peaks relative to that of the main (400)-reflection from having 1/6 of the site filled by Li, and even more so with Li occupying 1/3 of the site.
- **4b-site:** This site is vacant in the parent compound, and in Supporting Figure 2 it is seen that diffraction patterns are indistinguishable whether it is empty or filled with Li. The filling of this site, appears as a consequence of charge balance, either as Li when Li enters the 24d or as Ni when Ni enters the 4a-site. As we keep 4a filled by Mn throughout this refinement, the latter is not considered here and the site is locked to contain the Li necessary to obtain charge balance.

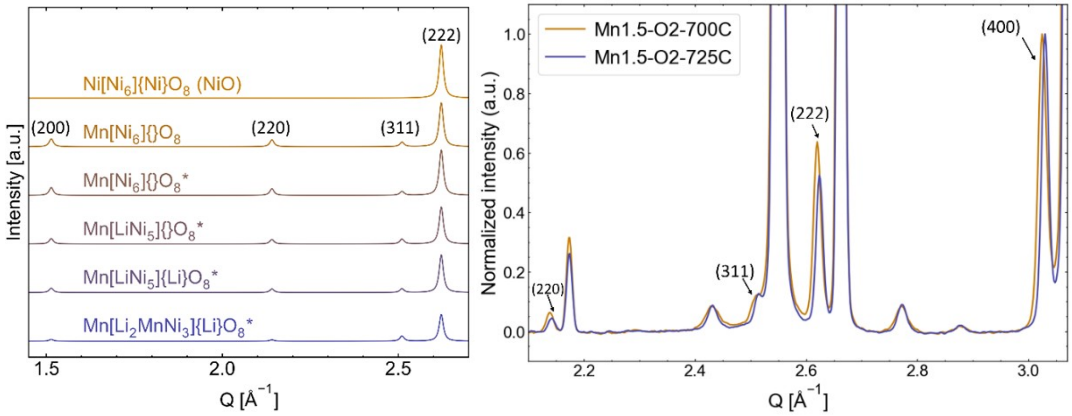

Supporting Figure 2 ***(Left panel)*** *Simulated X-ray diffractogram for six different rock salt structures. The ideal NiO-rock salt structure at the top, following different variants of the ordered $MnNi_6O_8$, with Mn at the 4a-site and varying occupancy of the 24d site , square brackets "[ ]", and the 4b site, curly brackets "{ }". *Here the rock salt phase has been simulated using a shifted oxygen position (x_O = 0.231 rather than 0.25).* ***(Right panel)*** *Two chosen samples with varying o-RS lattice parameters have been normalized after to the intensity of the RS (400)-reflection.*

In the right panel of Supporting Figure 2 two diffractograms are plotted after normalizing after the (400)-peak of the RS-phase. The sample annealed at 725 °C clearly has a smaller unit cell, and also a corresponding lowered intensity of both the (220)-peak and the (222)-peak relative to the sample annealed at 700 °C. This suggests that when lattice parameters is increasing, it is not only due to the introduction of a bigger atom in one or more of the sites, but this atom also seems to have a higher scattering factor. As can be seen in the left panel of Supporting Figure 2, the decreased intensity of (220) and (222) (whereas change of (311) is insignificant) can correspond with an increased Li-content in the 24d-site, which also would explain the lower lattice parameter.

Distance constrains:

Phase	Details on distance constrains
o-LMNO	This is the phase with the most known composition, based on previous ND/SXRD data from the research group we know the Mn-O bonds have very varying length, and each were given separate starting points of respectively 1.89 Å, 1.91 Å and 1.93 Å. With errors not kicking in until bond length exceeds 0.02 Å from these starting points, refinement allows for very ordered samples (large variations in bond distance) and not so ordered samples (more similar bond lengths). The Ni-O bonds were given wiggle room within the range 2.06 +/- 0.02 Å, whereas for the Li-O bonds this number was 1.96 +/- 0.05 Å.
d-LMNO	Based on the estimated Mn/Ni-ratio of this phase from lattice parameter considerations as explained in the article, and the estimated reference bond distances seen in the table above, penalties were implemented in the refinement when bond distances (Li – O and 16d – O) deviated more than 0.025 Å from the values given in Supporting Table 5.
e-LMNO	Due to the amount of Mn/Ni in tetrahedral sites, the lattice parameter is not expected to correlate well with the Mn/Ni-ratio of the 16d-site as in the d-LMNO case. Composition was set to 85 % Mn and 15 % Ni, which would mean 20 % Mn(III), 65 % Mn(IV) and 15 % Ni(II), assuming no oxygen vacancies and 8a filled with Li, for electronic neutrality (and simplicity). A larger wiggle room was applied for this phase, more specifically Li – O were allowed to be within 1.96 Å +/- 0.1 Å without penalties being applied, whereas 16d – O got to vary 0.06 Å from the estimated starting point of 1.953 Å.
o-RS	Due to the low intensity of this phase, and the large correlation of diffraction signal coming from Li in the 24d site and displacing the O sitting at the 24e-site (“O2”), a very strict constraint was put on 24d – O and the 4a – O distance, being only 0.001 Å from the calculated expected value. The 4b – O distance was on the other hand in practice not restrained, with distanced in the range 2.15 +/- 0.1 Å not being penalized. The reason for the latter is the likely presence of vacancies, strongly affecting this bond distance.
(N/M)-layered	Due to the severe overlap of this phase with e.g. the spinel phase, the estimated occupancies are not very well defined – and the estimated Mn/Ni-ratio is purely based on previously published phase diagrams. Still, bond distance constrains are added to help achieving at least plausible compositions. Both the 3a – O and 3b – O distance (calculated based on refined occupancies and estimated bond lengths seen in Supporting Table 5), is given wiggle room of +/- 0.025 Å.

Supporting Table 4 Going through each of the phases and how distance constrains have been implemented in the Rietveld refinement (using jEdit and Topas v6). For o-LMNO the starting points are based on experimental values, whereas in the other phases literature values (see Supporting Table 5 below) are used as starting point.

Bond	CN	Est. length	Source
Mn(IV) – O	6	1.903 Å	[1]
Mn(III) – O	4	1.901 Å	
Mn(III) – O	6	2.031 Å	
Ni(II) – O	4	1.95 Å	
Ni(II) – O	6	2.07 Å	
Li – O	6	2.15	[2]
Li – O	4	1.96	

Supporting Table 5 From literature certain bond distances were estimated and used as starting point in bond length estimations. These estimates combined with site occupancy refinements were used to calculate expected bond lengths.

Both the (310) and the (222) peak areas are found by fitting a Pseudo-voigt (PV) function to the spinel peak, and another PV to the neighboring, and sometimes overlapping, (222) rock salt peak. For high resolution data the spinel peak must be described using two PVs (one for d-LMNO and one for o-LMNO). For (310) a 2nd degree polynomial describes the background, and is fitted from approximately Q = 2.1 Å^{-1} to Q = 2.5 Å^{-1}, with an additional PV describing the right part of the region, where a new peak is emerging – namely (311) of the o-RS or the spinel phase. A 2nd degree polynomial is necessary in most samples, due to the decreasing nature of the background arising from the scattering of the amorphous glass capillary. For (222) a linear background is used to account for the full fitted region (from Q = 2.56 Å^{-1} to Q = 2.73Å^{-1}), and a PV is used to describe the left part of the region, arising from the right shoulder of the spinel (311)-peak.

Supporting Table 6 Description of fitting procedure for RO-calculations and domain size determination

Supporting results

Example of analysis of a complex multi-phased Li-Mn-Ni-O sample:

Here follows an example on how to properly characterize a sample with coexisting spinel-phases follows, using Mn1.6-500C as an example. The first step is **realizing that one spinel phase is not sufficient**. This is seen from doing an initial fit of the raw data, which exposes several features. From the top panel of Supporting Figure 3 it can be seen that (i) the peak asymmetry is not consistent with just one weakly ordered LMNO-phase in addition to a N-layered phase, and (ii) the d-values of the weak Mn/Ni superstructure peaks are shifted relative to the characteristic spinel peaks, suggesting that the ordered spinel phase has a shorter a-axis than in the fit. In addition, it can be seen in the bottom panel of Supporting Figure 3 that the (220)-reflection around Q = 2.17 Å^{-1} was also fitted bad, with too low intensity. This indicates that (iii) more heavy scattering atoms, like Mn, occupy tetrahedral sites. This is a feature known to be more dominant in disordered LMNO. Hence, there are solid evidence for coexistence of both o-LMNO and d-LMNO.

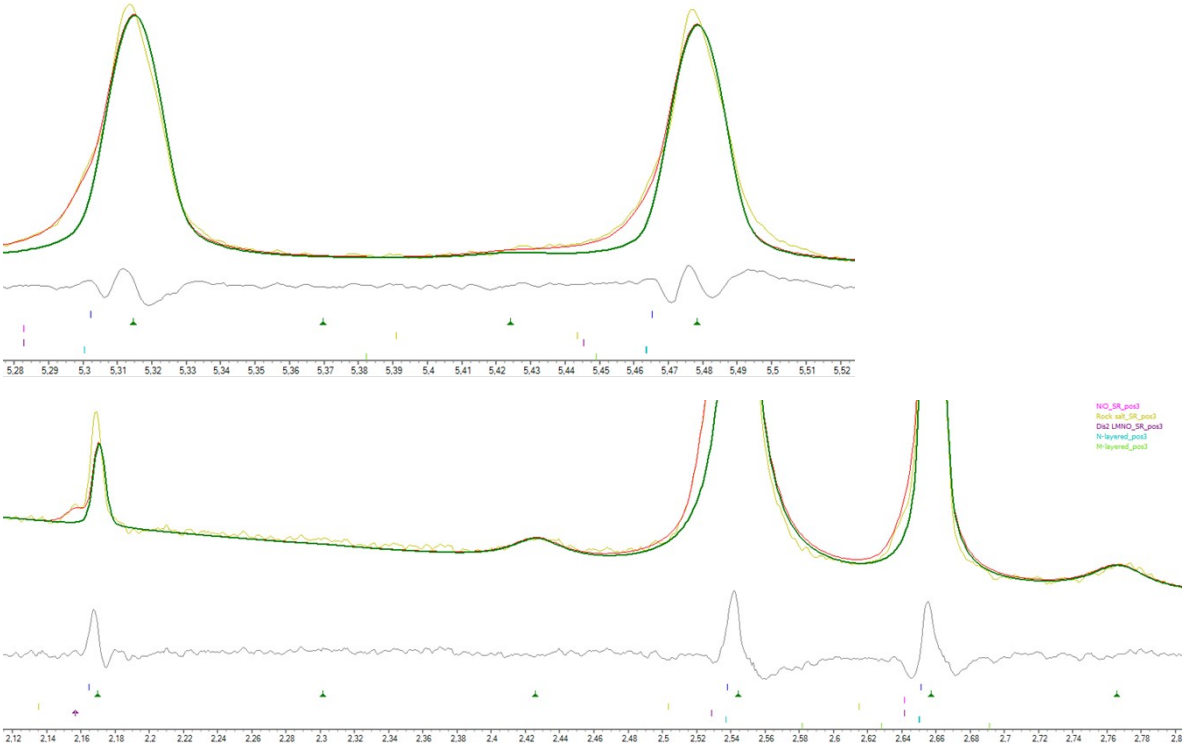

Supporting Figure 3 Preliminary refinement of SXRD data of Mn1.6-500, using only a o-LMNO phase (green) in addition to a N-layered phase. Log intensity used in both panels. ***(Top panel)*** *High Q-range peaks of Mn1.6-500, showing how one ordered phase cannot account for the asymmetry of the peaks. Furthermore a slightly too high lattice parameter is inflicted on the ordering peak around 5.43 Å^{-1}, (543)/(550)/(710)* ***(Bottom panel)*** *Lower Q reveals that the intensity of around 2.17 Å^{-1} (220) is too low due to lacking Mn in tetrahedral site in the refinement.*

The next step is to allow for both o-LMNO and d-LMNO, and then **refining the positions of the atoms in the o-LMNO phase.** Still, the o-LMNO phase is not satisfactory refined, see Supporting Figure 4. These initial fits are using the same atomic coordinates as the most ordered sample, Mn1.5-MO (Supporting Table 7), but intensities of the superstructure peaks are too, also influencing the peak shape. As the lattice parameter of o-LMNO is rather high for this sample it is likely slightly Mn-rich, and the Mn- and Ni-atomic coordinates are thus expected to be less displaced on average. After **allowing atomic positions to be refinement**, the fit of the superstructure peaks becomes satisfactory (Supporting Figure 5). A further optimization, and justification for the presence of N-layered phase and e-LMNO phase is continued in the main article.

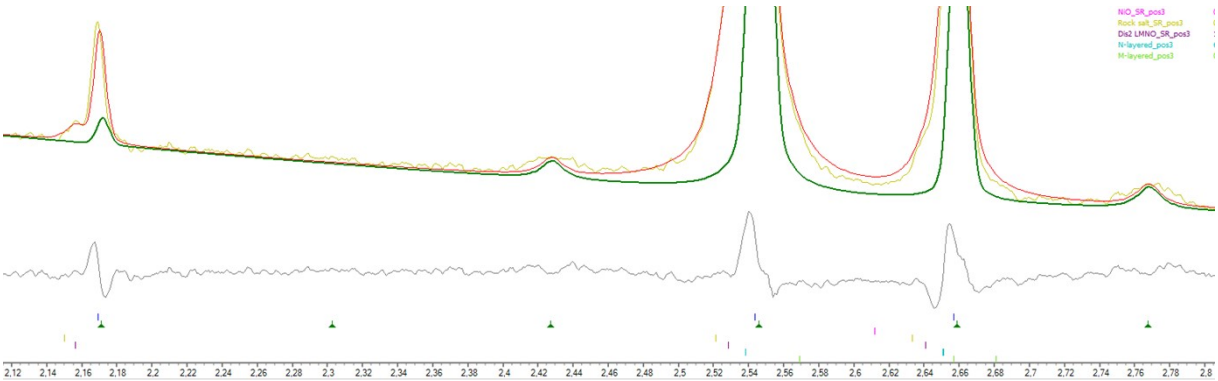

Supporting Figure 4 SXRD data of Mn16-500C fitted with two spinel phases, one ordered (green) and one disordered. (220)-peak at 2.17 Å^{-1} clearly better fitted than in Supporting Figure 3, but superstructure ordering peaks are not well fitted. Plotted with log intensity.

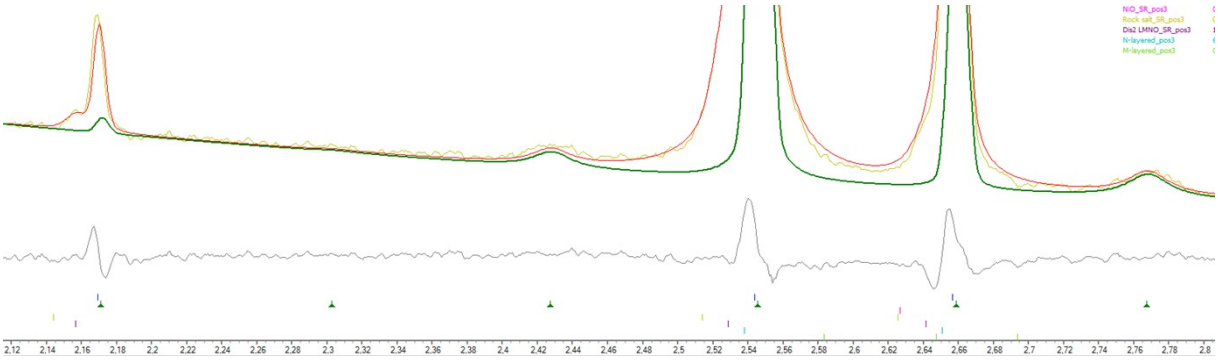

Supporting Figure 5 SXRD data of Mn16-500C fitted with two spinel phases, one ordered (green) and one disordered. Allowing the atomic coordinates of the ordered phase to refine, to properly account for the intensity of the supercell peaks at 2.42 Å^{-1} (310) and 2.77 Å^{-1} (320). Plotted with log intensity.

Atomic positions and bond distances in MO-samples

		Mn1.5-MO	Mn1.55-MO	Mn1.6-MO
o-LMNO	x8c	0.0009(**)	0.0005(**)	0.0009(**)
	y12d	0.3798(3)	0.3797(2)	0.3799(3)
	xO1	0.384(1)	0.3840(9)	0.384(1)
	xO2	0.1511(9)	0.1511(8)	0.1515(9)
	yO2	-0.144(1)	-0.1435(8)	-0.143(1)
	zO2	0.124(1)	0.1246(8)	0.125(1)
	Mn(12d)-O1(8c) x2	1.935(8)	1.935(7)	1.935(8)
	Mn(12d)-O2(24e) x2	1.873(8)	1.871(6)	1.870(7)
	Mn(12d)-O2(24e) x2	1.896(8)	1.900(7)	1.902(8)
	Ni(4a)-O2(24e) x 6	2.065(8)	2.063(7)	2.062(8)
	Li(8a)-O1(8c)	1.91(6)	1.90(5)	1.91(6)
	Li(8a)-O2(24e)	1.98(2)	1.98(2)	1.98(2)
d-LMNO	xO2	0.00(*)	0.265(3)	0.2644(6)
	M(16d)-O(32e)		1.93(2)	1.939(4)
	Li(8a)-O(32e)		1.99(4)	1.980(9)
e-LMNO	xO2	0.26(3)	0.26(3)	0.26(4)
	M(16d)-O(32e)	2.0(3)	2.0(3)	2.0(3)
	Li(8a)-O(32e)	2.0(5)	1.9(5)	1.9(6)
RS	xO2	0.2(1)	0.00(*)	0.00(*)
	Ni(24d)-O2(24e)	2.09(7)		
	Mn(4a)-O2(24e)	2(1)		
	Li(4b)-O2(24e)	2(1)		

Supporting Table 7 Results from refining MO-samples. (*) Sample value locked (not refined) in the refinement. (**) Error larger than the value itself.

Lattice-parameter relationship of LMNO from data in literature

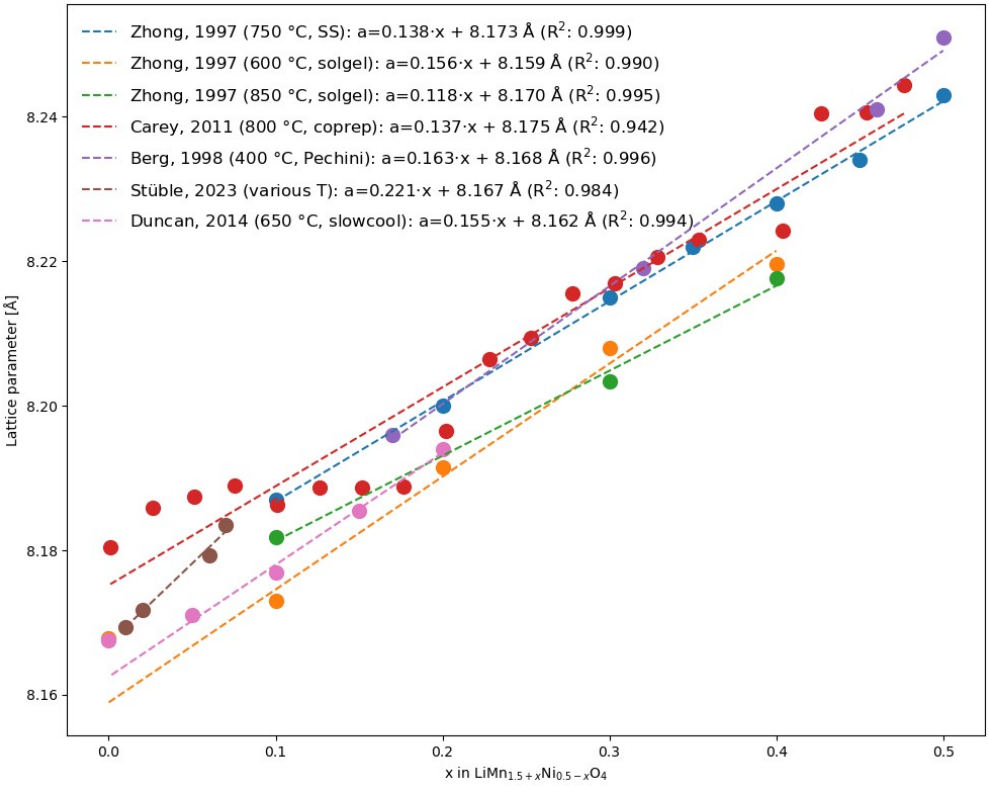

Supporting Figure 6 Data from various works[5–9] showing LMNO lattice parameter as a function of excess Mn in LMNO. Legend includes a short description of synthesis method followed by a linear fit of the data plotted in dashed lines of the same color.

Justification for allowing 8c-site refinement in o-LMNO of Mn1.5-MO

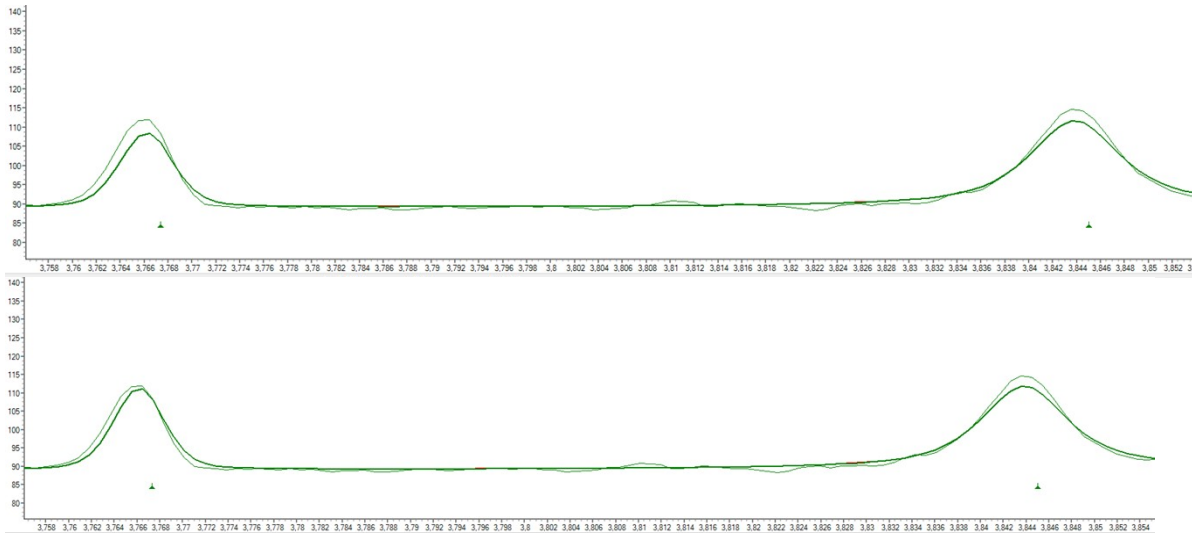

*Supporting Figure 7 Justification for allowing 8c-site of o-LMNO to be filled by Mn for Mn1.5-MO. **(Top panel)** 8c-site filled by 100% Li (R_{wp} = 5.747). **(Bottom panel)** After refinement, 0.6% of 8c site in o-LMNO filled by Mn (R_{pw} = 5.738). A marginal improvement seen best in the left peak, (422), at Q = 3.766 $Å^{-1}$.*

Lattice-parameter relationship of LizNiMn2-zO4, from data in literature[3]

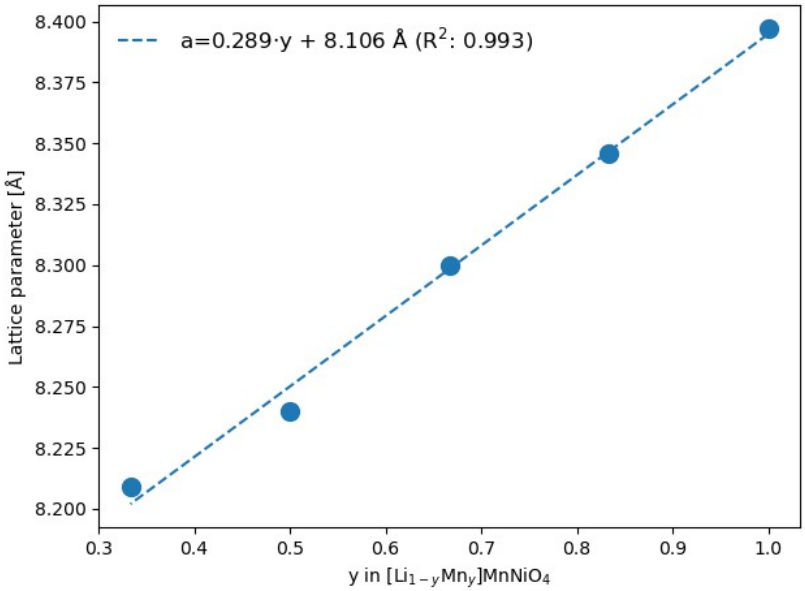

Supporting Figure 8 Lattice parameters reported by Feltz et al[3], together with their reported Mn-content I 8a-site. Linear interpolation from this is used to estimate composition of e-LMNO samples based on refined amount of Mn in 8a-site.

Justification for two spinel phases in Mn1.8-MO

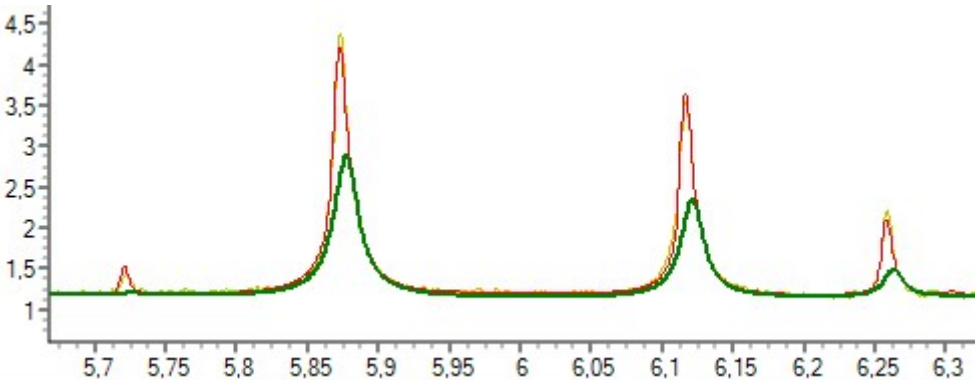

Supporting Figure 9 Justification for adding a second spinel phase to the Mn1.8-MO sample refinement, with a simple plot in the region Q ~ 5.65 – 6.35 Å^{-1}. The right shoulder is reasonably well fitted as a broad spinel with some strain. This is best visualized in the optimized detector position, at high Q and using a log scale, like in this figure, with intensity contribution of the low-angle spinel highlighted (green) together with total refinement (red) over the data (yellow).

Refinements of Q-samples

Rock salt: 14 well defined peaks, separated from spinel peaks

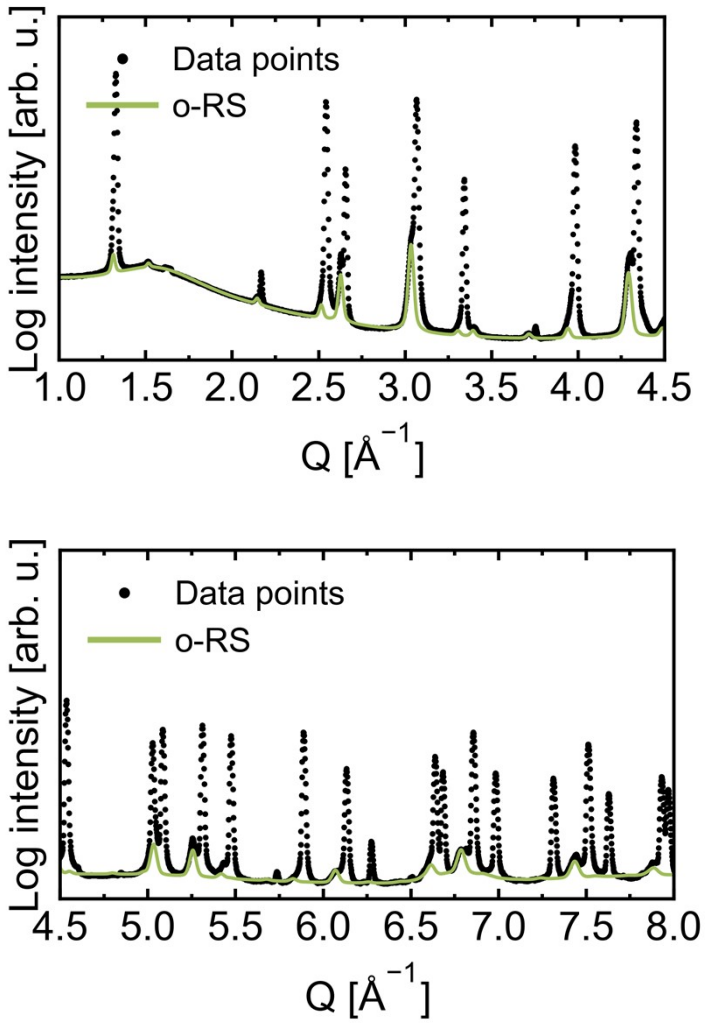

*Supporting Figure 10 Rietveld refinement showing that most RS-peaks are well separated from the spinel peaks when using high resolution instruments. Here exemplified using Mn1.5-Q as an example. Split up in two plots to better visualize the data, with **(top panel)** the lowest Q-values and **(bottom panel)** the highest Q-values. In total we argue that 14 of the peaks are separated sufficiently or have sufficient intensity, to confidently separate from the spinel peaks.*

Multiphased samples

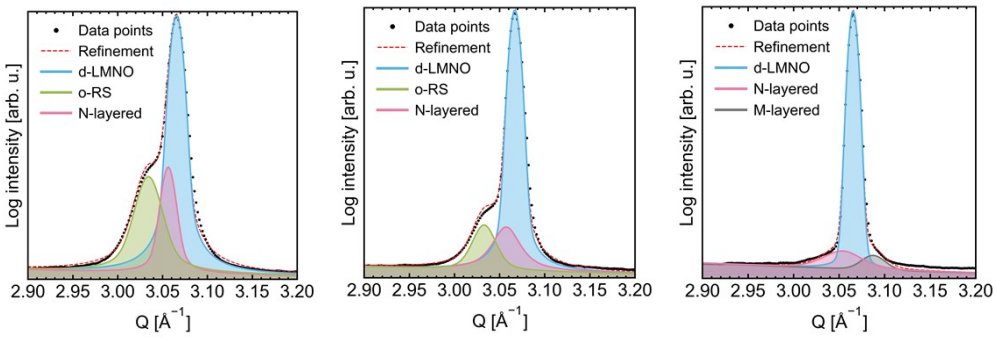

Supporting Figure 11 Rietveld refinements of ***(Left panel)*** *Mn1.5-Q,* ***(Middle panel)*** *Mn1.55-Q and* ***(Right panel)*** *Mn1.6-Q, showing the peak overlap etc.*

Testing different o-RS compositions to see how it affects the R_{wp}

To test which compositions of the rock salt are the best match to the diffraction data, rock salt compositions from work on the Li-Mn-Ni-O system has been used. That is two rock salt compositions suggested from the work of Rowe (quenching from 900 °C or 800 °C, in air) and one from McCalla *et al* (quenching from 800 °C in O_2). In the following refinements the overall stoichiometry are locked to literature values, but the site occupancies of the atoms are allowed to refine. The results can be seen in Supporting Table 8 alongside with the "free refinements", where stoichiometry is allowed to refine within the boundaries set by charge neutrality, as explained in the text. Even though the amount of Mn and Li is varying a lot in the different refinements, only minor differences are seen in the R_{wp}, which highlights that these occupational estimates are affiliated with rather large errors and is highly influenced by the oxygen position. These calculations are thus very sensitive to the bond length constraints (see "Experimental details" above). As expected, the o-RS phase has a similar lattice parameter and composition in Mn1.5-Q and Mn1.55-Q, so we thus assume the same composition for both. The best compromise (marked in bold in Supporting Table 8) seems to be the composition found from interpretation of the phase diagram of McCalla et al[4,5], quenched from the same temperature – even though heated in O_2-flow. Not only has it therefore been reported previously, it also fits well with the diffractogram and fulfills our charge neutrality principle. A visualization of the different refinement fits is seen in Supporting Figure 12.

Quench details	Composition and site occupancy	Mn1.5-Q		Mn1.55-Q		Source
		O (x,0,0)	R_{wp}	O (x,0,0)	R_{wp}	
900 °C in air	$Li_{0.35}Ni_{0.28}Mn_{0.37}$*: 24d: 8 ¾ Li, 7 Mn, 8 ¼ Ni 4b: 1 ¾ Li, 2 ¼ vac	0.23(1)	5.948	0.21(1)	4.996	
800 °C in air	$Li_{0.36}Ni_{0.34}Mn_{0.30}$*: 24d: 8 ¼ Li, 5 ¼ Mn, 10 ½ Ni 4b: 3 Li, 1 vac	0.23(1)	5.923	0.23(3)	5.54	6
800 °C in O_2	**$Li_{0.31}Ni_{0.50}Mn_{0.20}$*: 24d: 6.0 Li, 2 ¼ Mn, 15 ¾ Ni 4b: 3 ¾ Li, ¼ vac**	0.23(1)	5.870	0.22(2)	5.006	4,5
	$Li_{0.30}Ni_{0.50}Mn_{0.20}$**:	0.23(1)	5.881	0.23(3)	5.036	5

	24d: 6.1 Li, 2.2 Mn, 15.7 Ni 4b: 3.3 Li, 0.3 Ni, 0.4 vac					
800 °C in air (Mn1.5-Q)	$Li_{0.20}Ni_{0.57}Mn_{0.22}$: 24d: 4 ¼ Li, 2 ¾ Mn, 17 Ni 4b: 1 ½ Li, 2 ½ vac	0.23(1)	5.856	-	-	Refined in this work
800 °C in air (Mn1.55-Q)	$Li_{0.13}Ni_{0.67}Mn_{0.20}$: 24d: 2 ½ Li, 2.0 Mn, 19 ½ Ni 4b: ½ Li, 3 ½ vac	-	-	0.23(4)	5.036	

*Supporting Table 8 Showing results from refinement after locking the RS phase composition to several candidates found in literature. Bond distances are constrained according to what is explained above in the Supporting information, whereas the oxygen position of the phase(s) are presented in the table together with the corresponding R_{wp} from the refinement. In all cases the 4a-site is locked to be fully occupied by Mn(IV). In bold; the composition used to describe these samples. *Composition is read from reported phase diagram, and atoms are distributed according to the assumption made in the text. **Refinement from literature, plugging in the exact same atomic distribution within the phase*

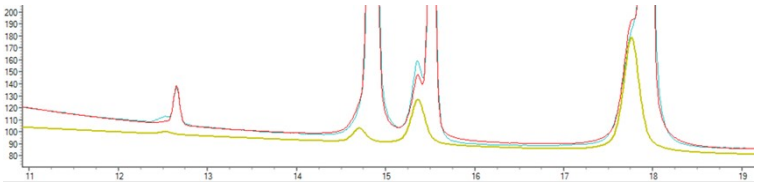

Refinement of Mn1.5-Q showcasing the RS-phase when site occupancies are locked to that suggested from visual interpretation of a previously reported pseudo-tertiary phase diagram of the Li-Mn-Ni-O system of a sample quenched from 900C in air (see Supporting Table 9).

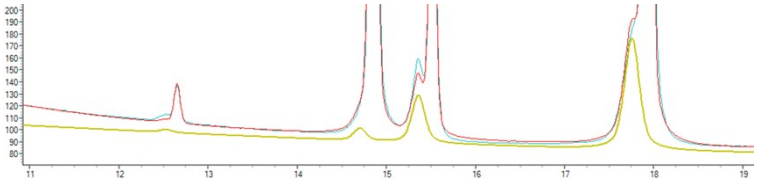

Refinement of Mn1.5-Q showcasing the RS-phase when site occupancies are locked to that suggested from visual interpretation of a previously reported pseudo-tertiary phase diagram of the Li-Mn-Ni-O system of a sample quenched from 800C in air (see Supporting Table 10).

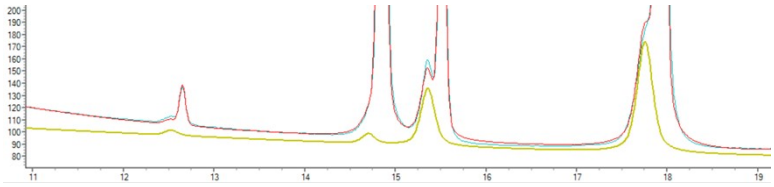

Refinement of Mn1.5-Q showcasing the RS-phase when site occupancies are locked to that suggested from visual interpretation of a previously reported pseudo-tertiary phase diagram of the Li-Mn-Ni-O system of a sample quenched from 800C in O_2 (see Supporting Table 11).

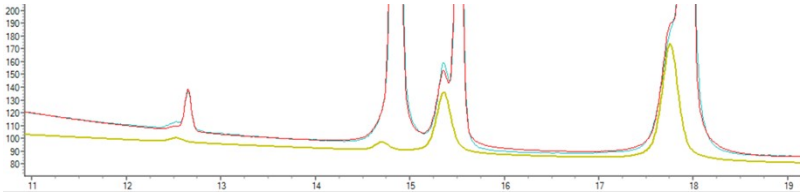

Refinement of Mn1.5-Q showcasing the RS-phase when site occupancies are locked to that suggested from visual interpretation of a previously reported refinement of a rock salt phase from a sample quenched from 800C in air (see Supporting Table 12).

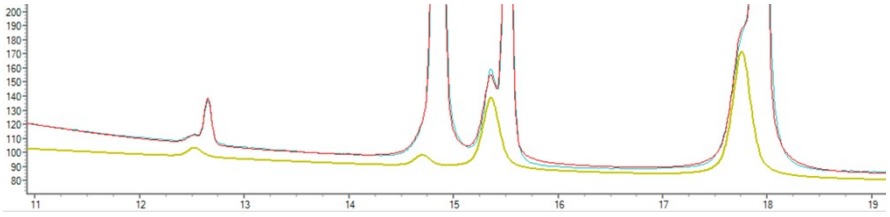

Refinement of Mn1.5-Q showcasing the RS-phase when site occupancies are refined, with charge neutrality as a constraint (see Supporting Table 13).

Supporting Figure 12 Illustration of the different ways of estimating the site occupancies of the RS phase in Mn1.5-Q (see Supporting Table 14)

Justification for refining without O-vacancies

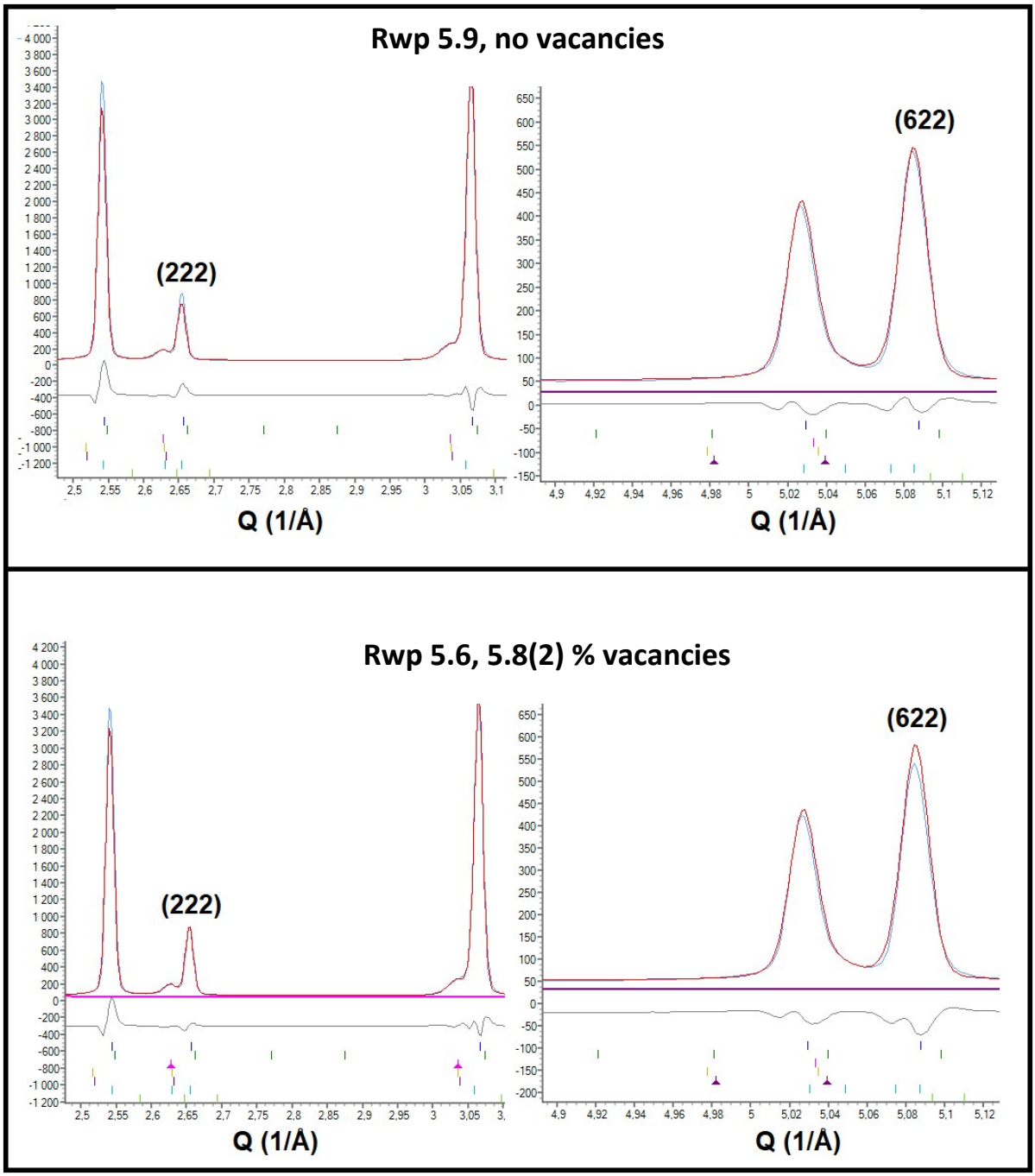

Supporting Figure 13 Refining without (top) and with (bottom) allowing for oxygen vacancies in the d-LMNO phase of Mn1.5-Q. Even though the R_{wp} improves, the difference in the calculated patterns are not convincing enough for us to proceed with this approach. All parameters of the d-LMNO phase are kept constant except the O-occupancy, and whereas the effect is positive on (222), where intensity increases to a better fit, O-vacancies also lead to a slightly too high intensity on the (622)-peak.

Phase overviews (annealed in air) with weighted spinel lattice parameters

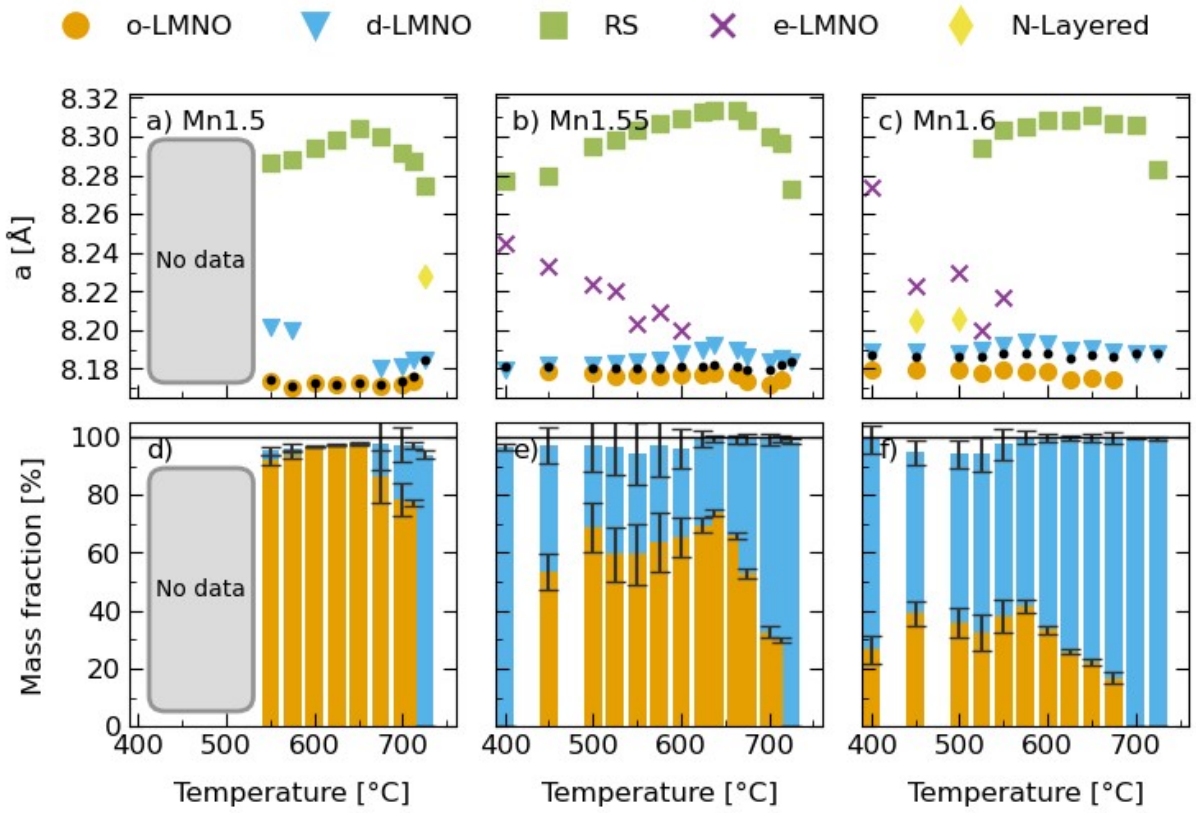

Supporting Figure 14 *Cubic (or pseudocubic for the N-layered phase) unit cell dimensions of samples annealed in* ***air*** *at temperatures between 400 and 750 °C, for* ***(a)*** *Mn1.5-,* ***(b)*** *Mn1.55- and* ***(c)*** *Mn1.6-samples. The corresponding mass fractions of the two main spinel phases, d-LMNO and o-LMNO are respectively in* ***(d)***, ***(e)*** *and* ***(f)****. Here, the small deviation from 100% reflects impurities, typically < 5 wt%, see below. Black dots represents the weighted average of the spinel phase lattice parameters. This illustrates that the overall spinel composition is rather consistent, mostly affected by impurity precipitation.*

Phase overviews (annealed in O_2) with weighted spinel lattice parameters

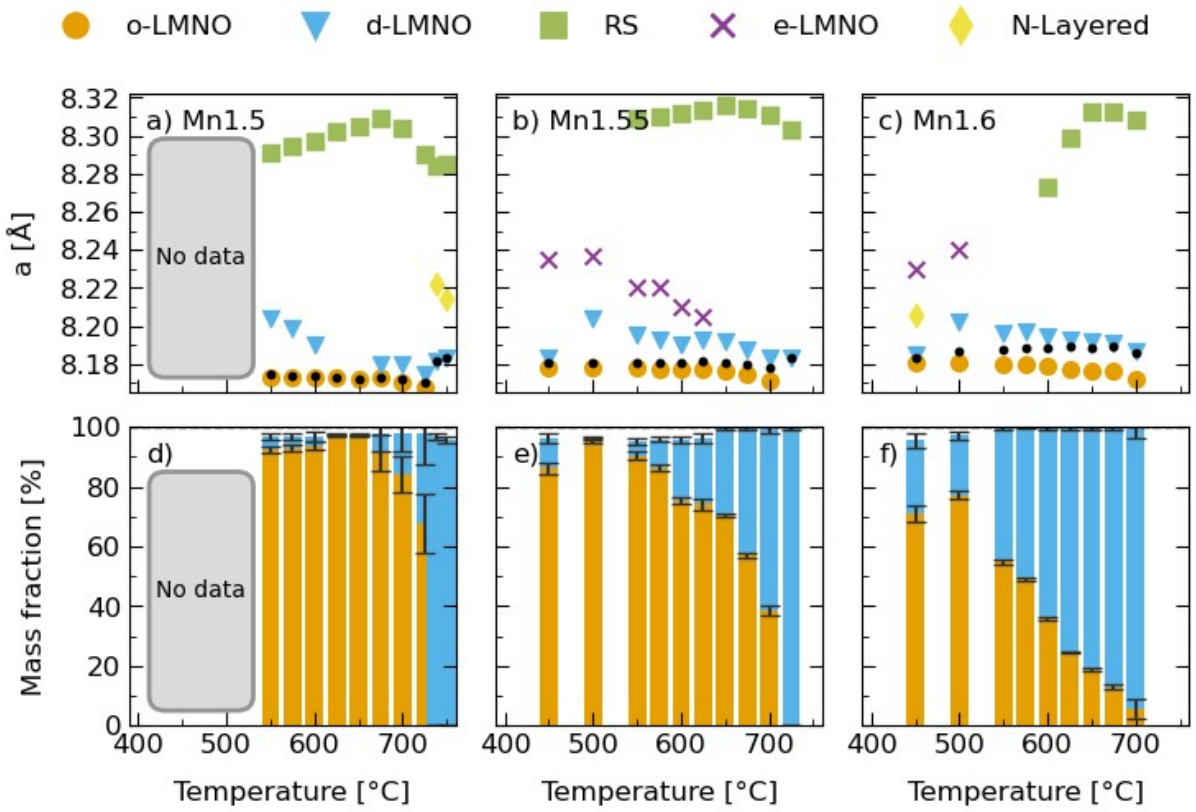

Supporting Figure 15 Copy of Figure 5 in the paper, only with the addition of black dots showing the weighted average of the spinel phase lattice parameters. This illustrates that the overall spinel composition is rather consistent, mostly affected by impurity precipitation.

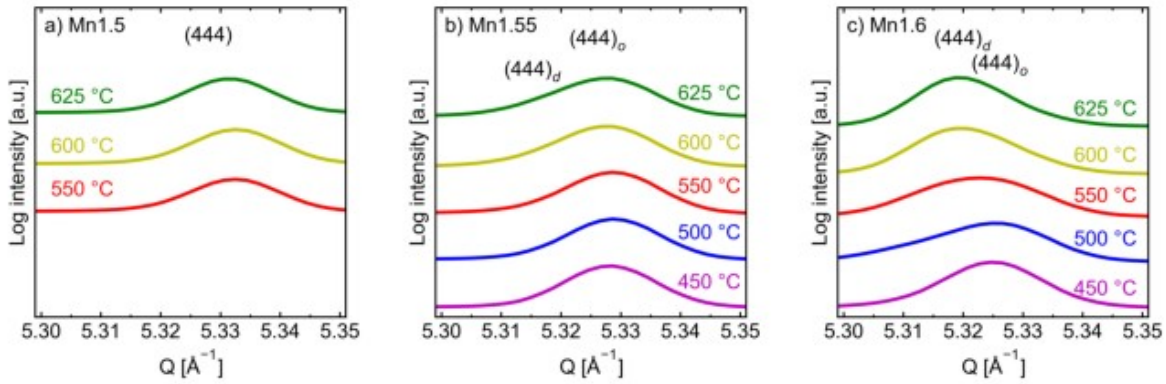

Supporting Figure 16 Figure showing how much more difficult it is to see peak splitting when measured with the non-optimized detector position, as compared to the optimized detector position in Figure 6.

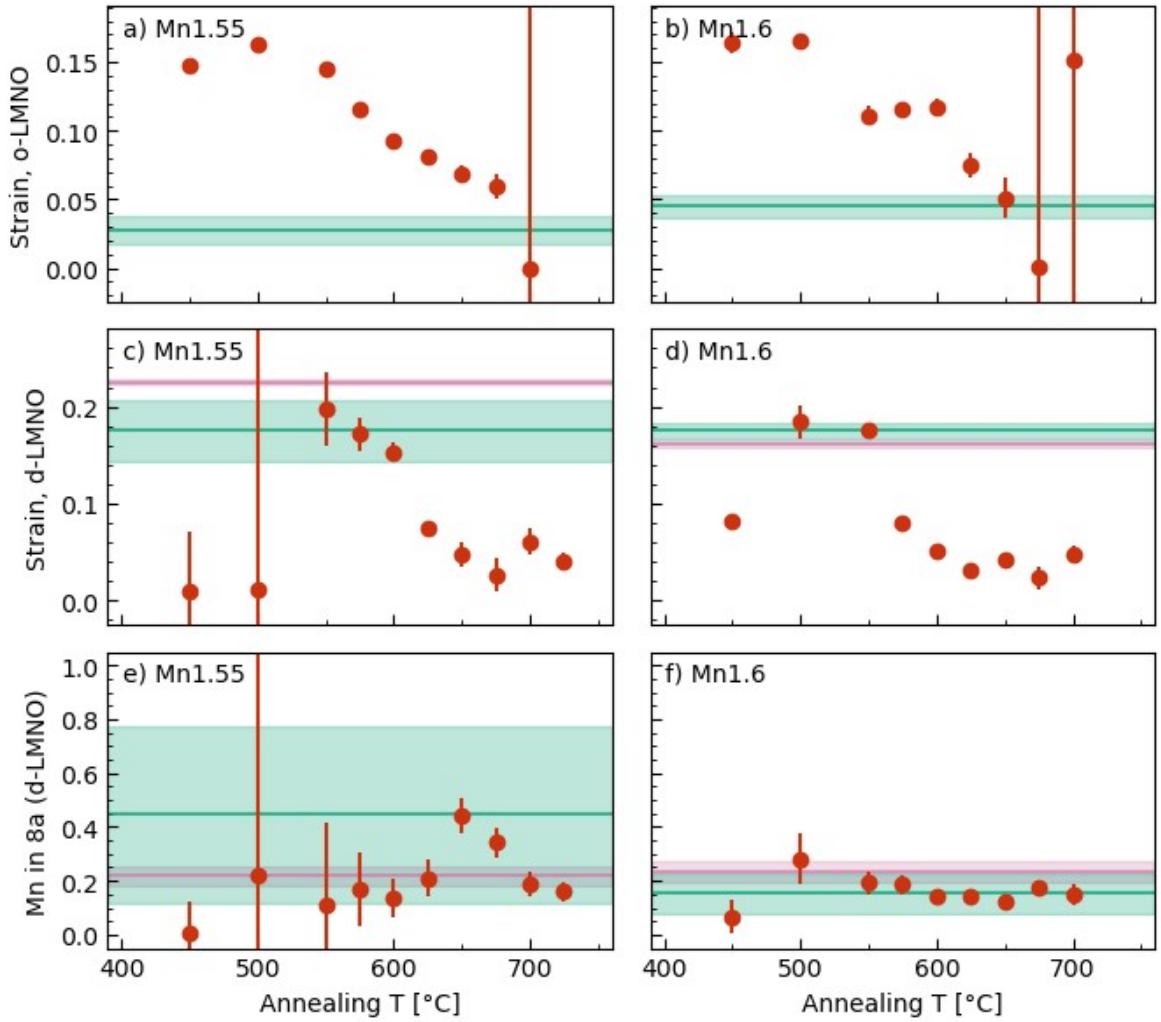

*Supporting Figure 17 Strain in the Mn-rich samples for **(a,b)** the o-LMNO phase and **(c,d)** the d-LMNO phase. The o-LMNO strain decrease after higher temperature annealing, whereas for d-LMNO it seems to have a maximum where the ordering is highest, around 550-600 °C for Mn1.55 and around 500-550 °C for Mn1.6. This thus does not support the theory of ordering being increased due to a more stable d-LMNO configuration in these samples – as the increased ordering seems to increase strain in the d-LMNO phase. In **(e,f)** the refined* occupancies of Mn/Ni at 8a-site in d-LMNO is shown for the same Mn-rich samples. The MO-samples (green line) are prone to large uncertainties (green shade) due to the small mass fraction of this phase, whereas the Q-samples are shown in red.

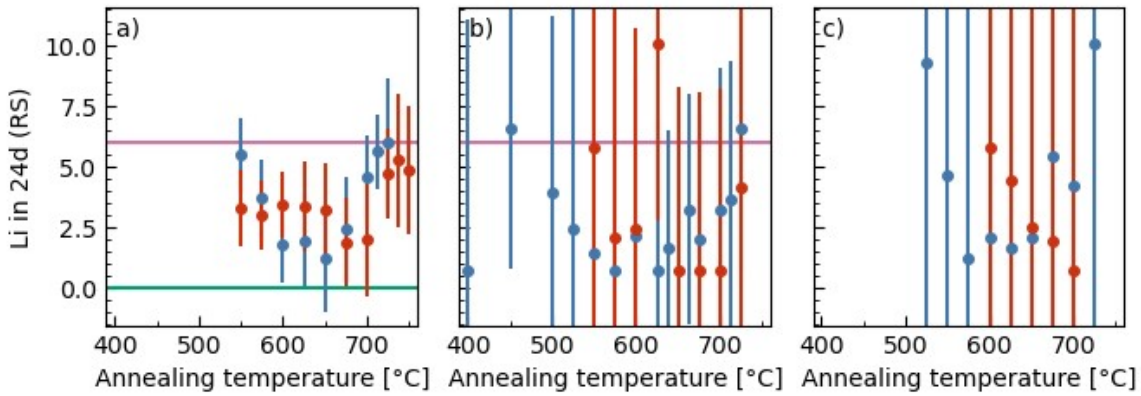

*Supporting Figure 18 Refinenemt results of the Li-occupation of the 24d-site in the o-RS phase of **(a)** Mn1.5-, **(b)** Mn1.55- and **(c)** Mn1.6-samples. Because of the low mass fraction of o-RS in the Mn-rich samples, these values are very prone to errors.*

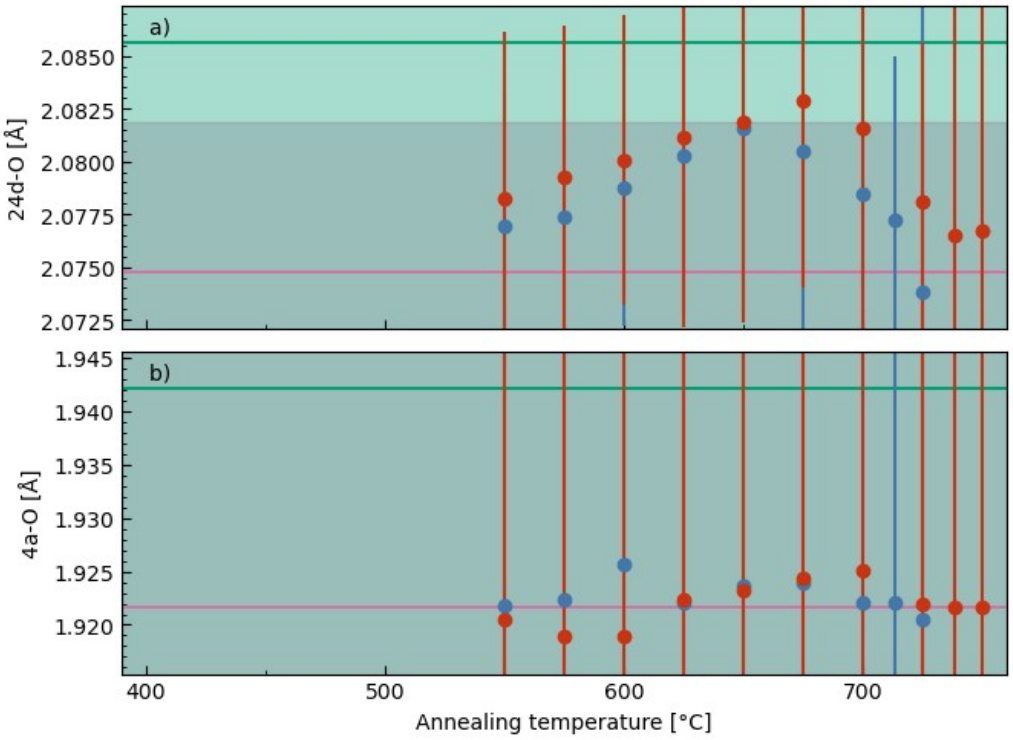

Supporting Figure 19 Calculated bond lengths between the 24d-site and oxygen for the Mn1.5-samples annealed at different temperatures in either O_2-flow (red) or static air (blue). The cation – oxygen bond distances differ for the various sites, and the 4a-O and 24d-O bond distances are plotted for the Mn1.5-samples. A rather clear trend for the 24d-site, whereas this is not the case for the 4a-O, where refinements are prone to even larger uncertainties. Bond lengths are as mentioned constrained to some extent, so one cannot conclude too much from this – nevertheless the result does strengthen the assumption, that lattice parameter variations are dominated by Li-content variations in the 24d-site.

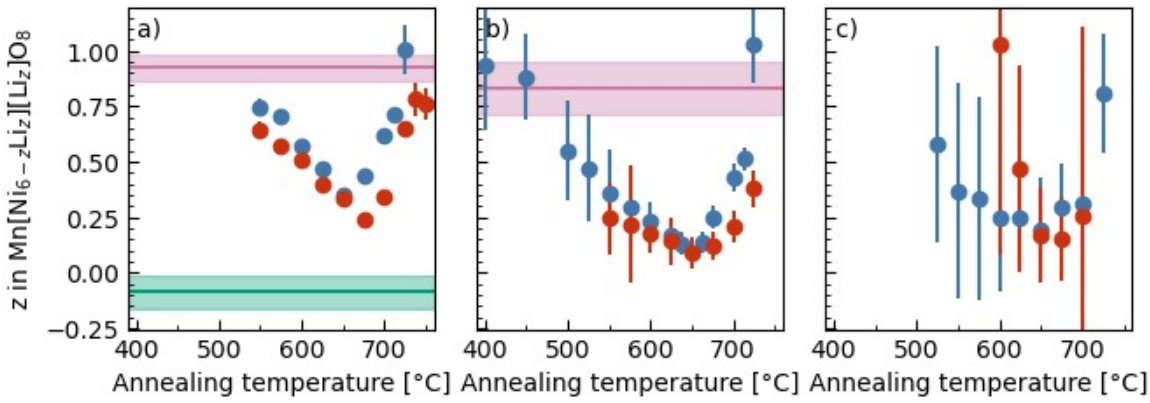

*Supporting Figure 20 T**he results of applying the relation in eq. 4 to the data set to estimate composition of o-RS is seen for **(a)** Mn1.5-, **(b)** Mn1.55 and **(c)** Mn1.6-samples. Most data points are giving sensible and realistic compositions as all values are within the realistic range of 0 < z < 1 except Mn1.5-MO (z < 0, which we already suggested must contain less Mn than the parent compound due to a lattice parameter higher than 8.32 Å) and some of the samples with very little o-RS (z > 1), prone to large errors.*

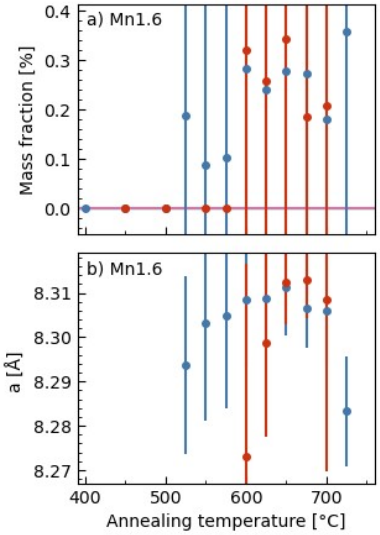

*Supporting Figure 21 **(a)** Mass fractions and **(b)** lattice parameter values for the o-RS phase of Mn1.6, analogous to Figure 8 in the paper. Due to the small mass fractions, also lattice parameter values are very prone to errors. Still – the lattice parameter trend seems clear. Multiplying the error value by 3 (as explained in Experimental) might not be the right approach for this data.*

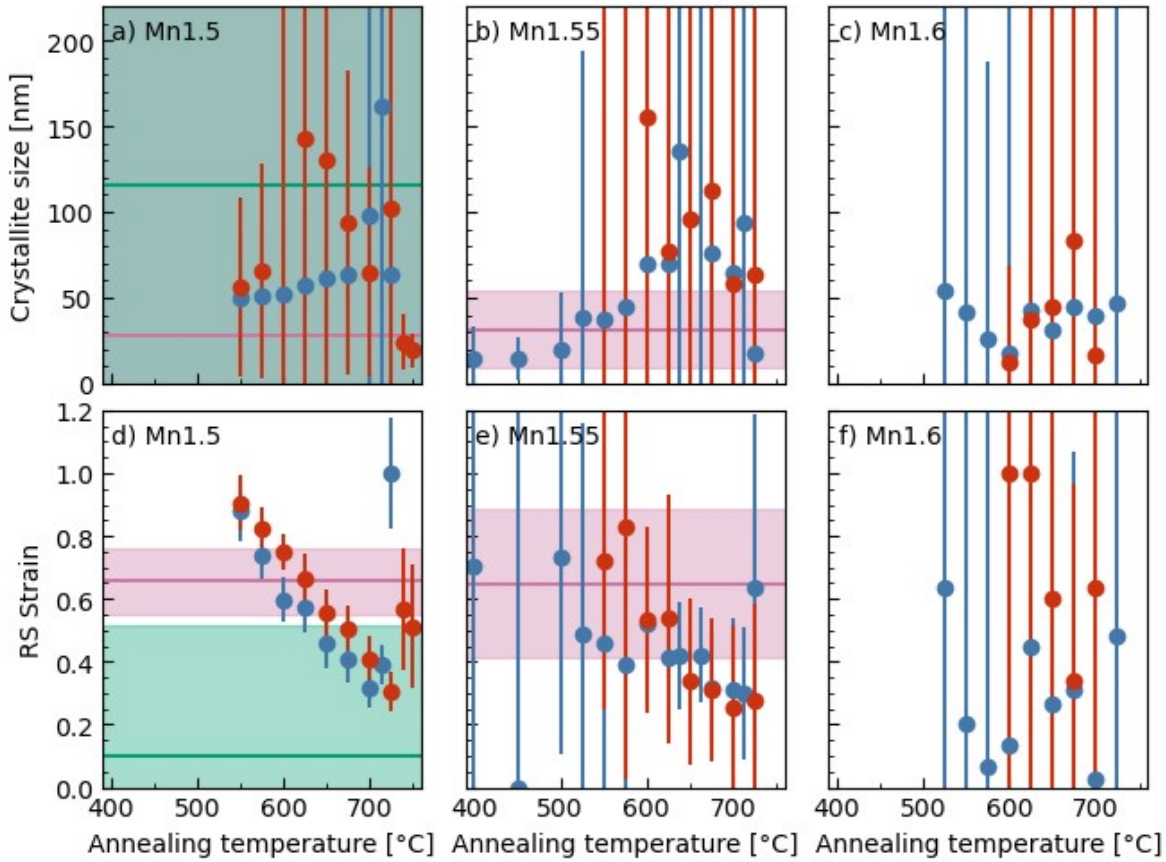

Supporting Figure 22 ***(a,b,c)*** *Estimated o-RS crystallite size for Mn1.5, Mn1.55 and Mn1.6-samples annealed 6 h as well as the corresponding* ***(d,e,f)*** *strain of the o-RS phase. The pink horizontal line represents status for the quenched starting material, the green horizontal line refers to the maximum ordered (MO) sample. Especially for Mn-rich samples (with little o-RS) errors are dominating the refinements.*

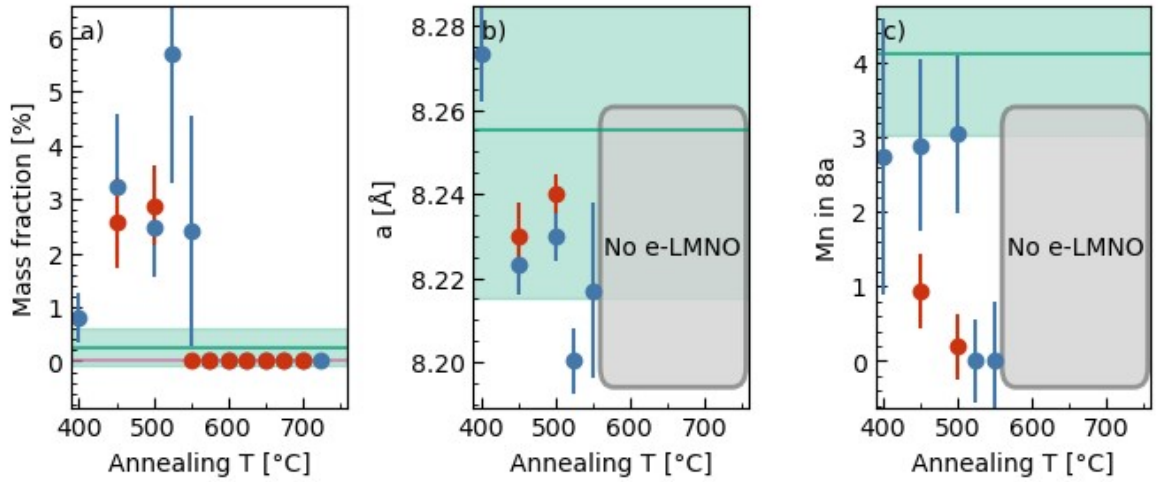

Supporting Figure 23 Refined values for e-LMNO in Mn1.6-samples. Namely ***(a)*** *mass fraction,* ***(b)*** *lattice parameter and* ***(c)*** *amount of Mn in tetrahedral 8a-sites. Figure comparable to Figure 9 in paper.*

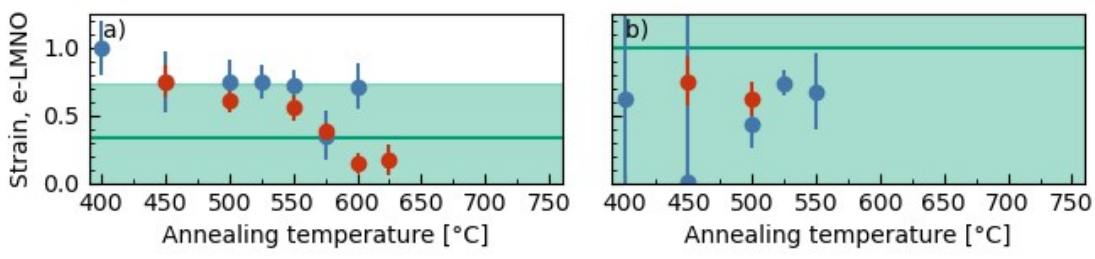

*Supporting Figure 24 Strain of the e-LMNO phase in **(a)** Mn1.55- and **(b)** Mn1.6-samples. In the former the phase is much more prominent, and errors are smaller.*

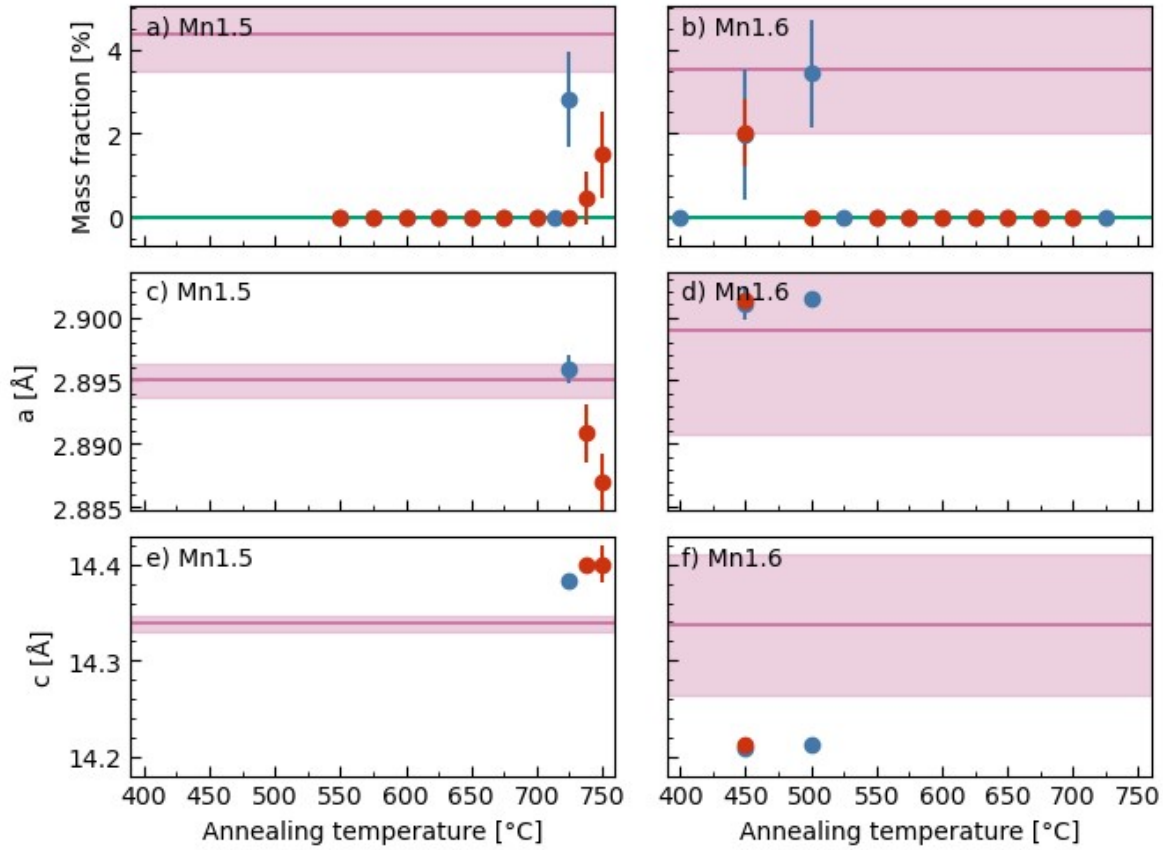

Supporting Figure 25 Refinement details from the refinement of the N-layered phase in Mn1.5- and Mn1.6-samples, with **(a,b)** mass fractions, **(c,d)** a-axis and **(e,f)** c-axis. The colored regions represent estimated errors and comparison with reference samples; Q- (pink) and MO-samples (green).

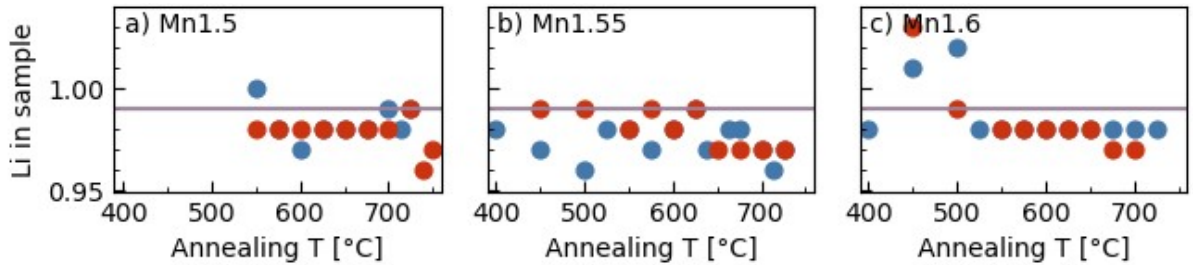

Supporting Figure 26 Estimated sample stoichiometries based on the refinement of every annealed sample, as compared to the Q (pink) and MO (green) samples. NB: When value for the Q- and MO-sample is identical it appears as gray due to color mixing. The black dashed line represents the expected amount from ICP.

Raman

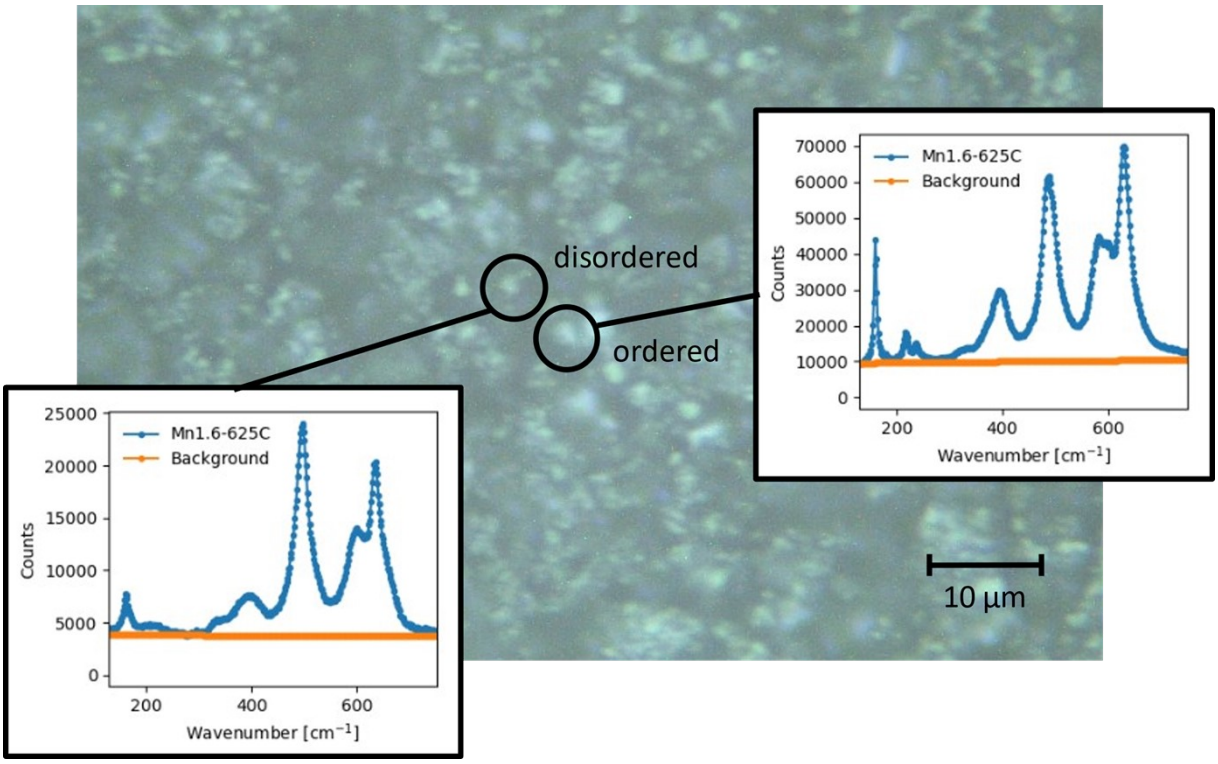

Supporting Figure 27 Example of two spots on the same sample (Mn1.6-625C) showing very different degree of order, one disordered whereas the other clearly ordered.

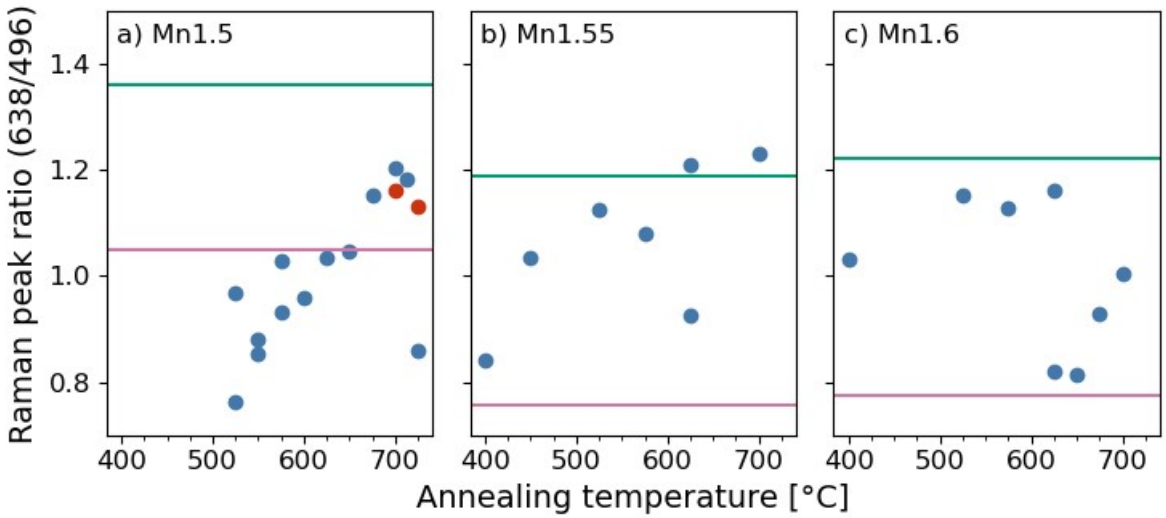

Supporting Figure 28 Intensity ratio of the maximum intensity around 638 cm^{-1} and that around 496 cm^{-1}. Similar to Figure 13 in paper, only using a different peak ratio. Corresponding MO-sample shown with a green line, and Q-sample with a pink line.

Identified Raman modes and discrepancies form other reports

Wavenumber (cm^{-1})	Comment
~170-180	There is a peak around 180 cm^{-1} which is not present in the Raman spectra presented by Stüble *et al*. According to the work of Miwa *et al* could be ascribed to a T_2-mode around 179 cm^{-1}.[8] However, this same mode seems to be ascribed to the peak around 171 cm^{-1} in Stüble's work, whereas in the MO-samples there is a separate peak at this frequency. The nature of this mode around 170 cm^{-1} is thus inconclusive.
~250	The peak around 250 cm^{-1} (possibly an E-mode[8]) is much more intense in the MO-samples than Stübles samples.
~325	The peak around 325 cm^{-1} (E-mode[8]) is much more intense in the MO-samples than Stübles samples.
~340	The T_2-mode[8] around 340 cm^{-1} is visible in the MO-samples, but not in Stüble's work.
~470-490	Peaks at 478 cm^{-1} and 486 cm^{-1} are more prominent for Stüble's samples, ascribed to TO/LO-modes[8]. There is however a left shoulder arising on the huge A-mode peak around 500 cm^{-1} for the MO-samples, but it seems more likely these arise from the T_2-modes (482 and 485 cm^{-1}).
~552	This TO-mode[8] seems to be present in both Stüble and MO-samples, though not specifically mentioned by Stüble *et al* in their report.
~580-620	The peak cluster around 600 cm^{-1} is split in three very distinct peaks corresponding to T_2-modes. in the MO-samples, around 580, 594 and 614 cm^{-1}, corresponding to literature.[8] This is similar, but not identical to, what is reported by Stüble *et al* - where peaks are assigned to 584, 596 and 613 cm^{-1}.

Supporting Table 9 As compared to the great work of Stüble et al[7], some differences occur in the Raman spectra which we would like to highlight as these works presents some of the most ordered LMNO samples in literature. Some peaks only exist in some of the samples, whereas other peaks have rather large (relative) intensity differences. Important to note that assignment of Raman modes is not part of our expertise. We therefore do not discuss the validity of these assignment.

Supporting Table 10 Experimental details of synthesis, electrode preparation, cell fabrication and testing parameters for the data presented in Supporting Figure 29 below, providing the relative electrochemical capacity contribution from Mn-activity in the different stoichiometries.

	Mn1.5, Mn1.6, Mn1.7, Mn1.8, Mn1.9)-EC
Synthesis	The samples of various stoichiometry (Mn1.5, Mn1.6, Mn1.7, Mn1.8, Mn1.9) are named "EC" to point out the samples were tested electrochemically: After undergoing the modified Pechini method as described in the article, the samples are heated at 900 °C for 10 h, followed by cooling (5 °C/min, except for Mn1.8 that were set to 10 °C/min) to 700 °C and annealing there for 10 h before cooling at the same rate. Thereafter the muffle furnace is turned off and the sample is kept inside the muffle to cool.
Electrode cast	Electrodes were prepared using NMP (Sigma-Aldrich) based slurries containing active material powders (80 wt% LMNO), conductive agent (10 wt% Super P, TIMCAL/Imerys) binder (10 wt% PVDF, Arkema Kynar HSV1810). A centrifugal mixer (Thinky, Co., ARE-250CE) was used first to dissolve the binder, and then to homogenously mix it with the LMNO and super P. Next the slurry was tape casted on 15 µm Al-foil. After drying overnight inside fume hood, the electrodes were punched into discs (15 mm diameter) and dried at 80 °C under dynamic vacuum in a Büchi oven overnight and kept inside the glovebox for cell assembly. Due to differences in wet thickness the loading in the end is varying quite a lot from stoichiometry to stoichiometry. Average loading is 5.0 mg/cm^2 (Mn1.5-EC), 1.6 mg/cm^2 (Mn1.6-EC), 2.2 mg/cm^2 (Mn1.7-EC), 3.3 mg/cm^2 (Mn1.8-EC), 1.9 mg/cm^2 (Mn1.9-EC).
Cell assembly	All coin cells were assembled and tested in half-cell configuration in CR2032 stainless steel (SS316) cases from PI-KEM. Cells were assembled inside an argon-filled glovebox, and consisted of a lithium metal disk (MTI), a glass fibre separator (Whattman), electrode discs prepared as described above, a stainless steel spacer and washer. Commercial LP30 (Sigma–Aldrich) was used as electrolyte. Three coin cells from each stoichiometry was made and tested, but for Mn1.6 and Mn1.9 one of the cells were discarded due to malfunction and only two are added in Supporting Figure 29.
Electrochemical cycling	Details in caption of Supporting Figure 29.

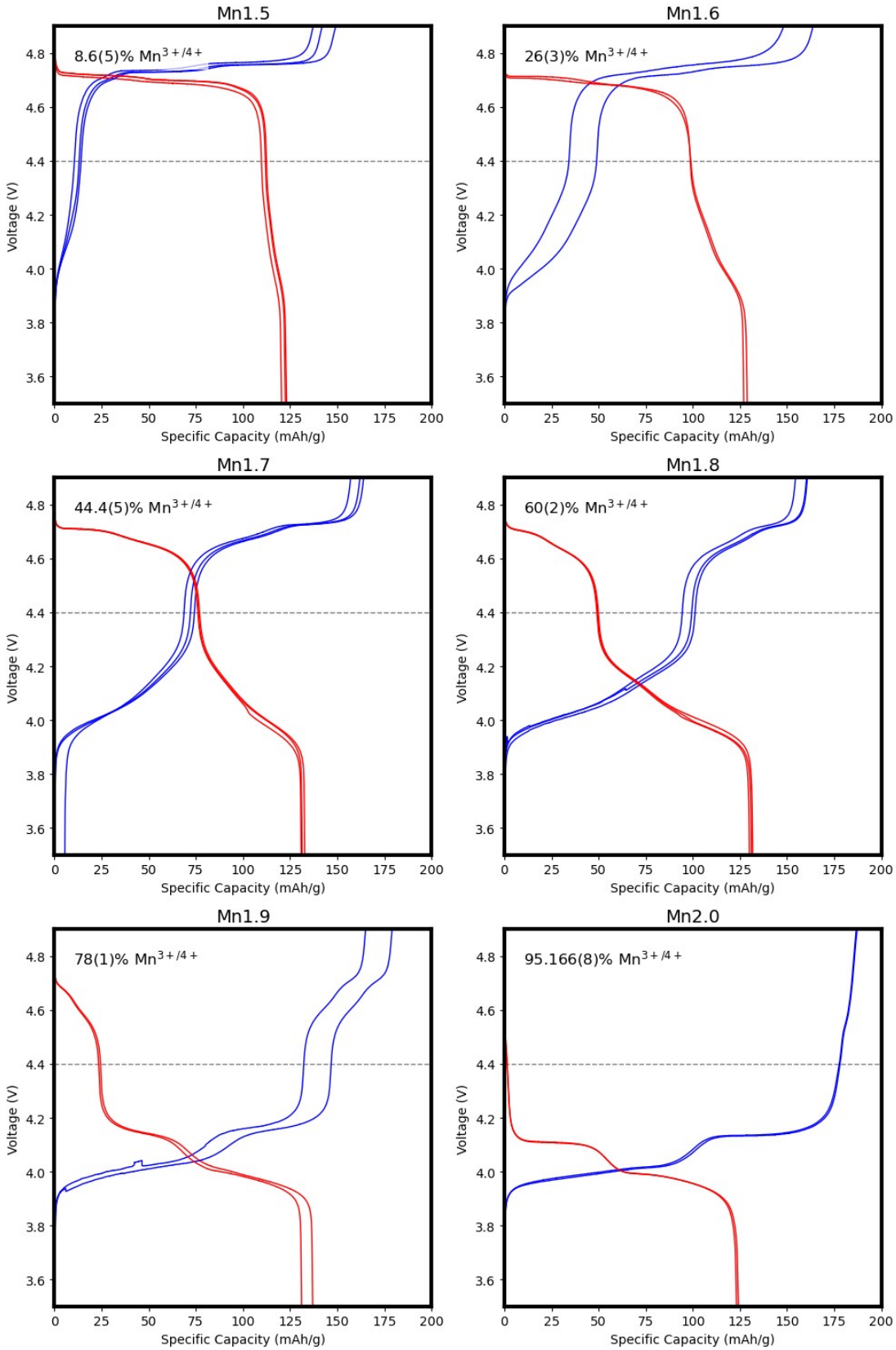

Supporting Figure 29 First charge/discharge of cells having different stoichiometries (Mn1.5-Mn1.9)-EC. Cycled at C/10 between 3.5 – 4.9 V vs Li/Li⁺. A BTS4000 cycler (Neware) was used. The ratio of the first charge capacity below 4.4 V (from $Mn^{3+/4+}$) and the full first charge capacity is written in the plot, with standard error. Even though LMNO loading varies from stoichiometry to stoichiometry (see Supporting Table 9), we believe at these slow cycling speeds this should not matter having such a high amount of conductive agent (10 wt%). The expected values based on phase pure and ideal samples of these samples would be 0%, 20%, 40%, 60% and 80% for Mn1.5, Mn1.6, Mn1.7, Mn1.8 and Mn1.9 respectively.

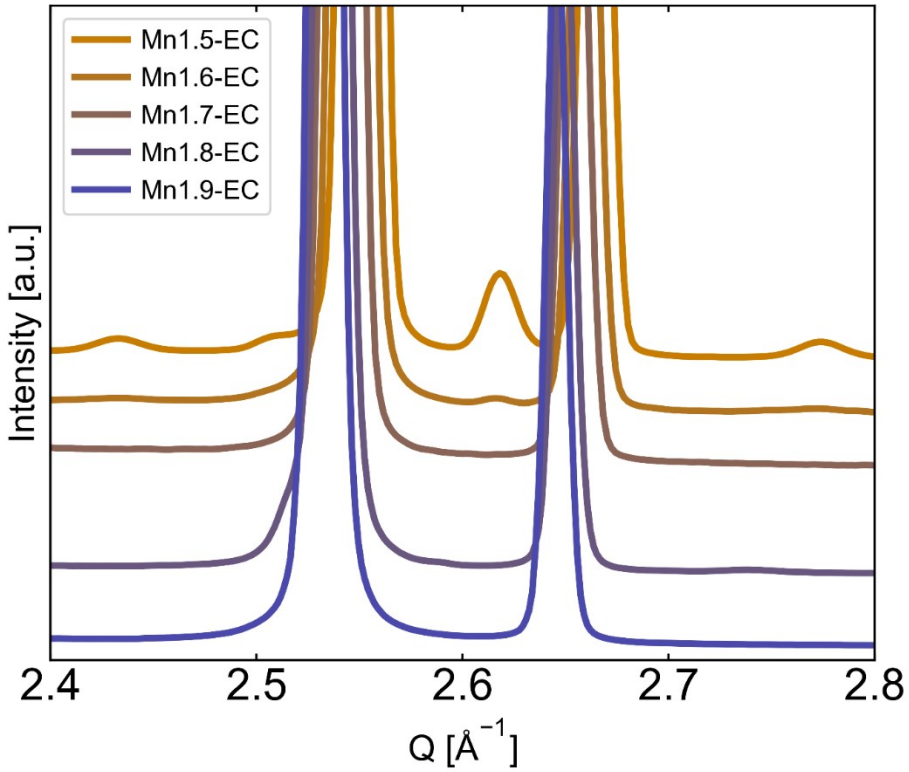

Supporting Figure 30 SXRD data of the samples tested electrochemically as seen in Supporting Figure 29. Rock salt impurity prominently present for Mn1.5-sample ((311)-peak at ~2.5 Å^{-1} and (222)-peak ~2.6 Å^{-1}), and in small quantities for the Mn1.6-sample. Ordering can also be observed for the Mn1.5-sample (the (310)-peak around 2.42 Å^{-1}and (320)-peak around ~2.78 Å^{-1}) and to a very small extent also for the Mn1.6-sample.

Mn1.6-500C-72h, deep discharge experiment(s)	
Synthesis	After undergoing the modified Pechini method as described in the article, the samples are heated at 900 °C for 10 h, followed by quenching. After grinding, sample is reheated at 500 °C in O_2-flow (20 mL/min) for 72 h. A thorough material characterization of this sample will be the focus of a future paper by the authors.
Electrode cast	Same as in Supporting Table 10, only using different mixing rations; active material powders (92 wt% LMNO), conductive agent (4 wt% Super P, TIMCAL/Imerys) binder (4 wt% PVDF, Arkema Kynar HSV1810). Loading of electrode used in Fig 14a and b is 3.37 mg/cm^2 (for parallel cell in 14b it is 4.727 mg/cm^2), whereas for operando cell in 14c it was 3.53 mg/cm^2.
Cell assembly	**For coin cells:** Same as in Supporting Table 10, only using LP40 as electrolyte and an improved separator (WhatMan QMA Quartz Microfiber Filters CAT No. 1851-865) and two stainless steel spacers rather than one. **For operando cells:** As mentioned in article, cells are custom made, but based on those designed by Drozhzhin et al – only using glassy carbon windows rather than sapphire. Using LP40 electrolyte and QMA-separators, in addition to two Li-metal discs to ensure good physical contact inside the cell.
Electrochem. cycling	Coin cell data in Figure 14a collected on a BTS4000 cycler (Neware), 50 cycles (1.5 V – 5.0 V) at C/8, to mimic the operando experiment. **Operando** data acquired at C/8 using a portable BAT-SMALL cycler (Astrol Electronic AG), also cycling 1.5 - 5.0 V.

Supporting Table 11 Experimental details of synthesis, electrode preparation, cell fabrication and testing parameters for the coin cell data and operando data presented in Figure 14 in the article, and Supporting Figure 33 below.

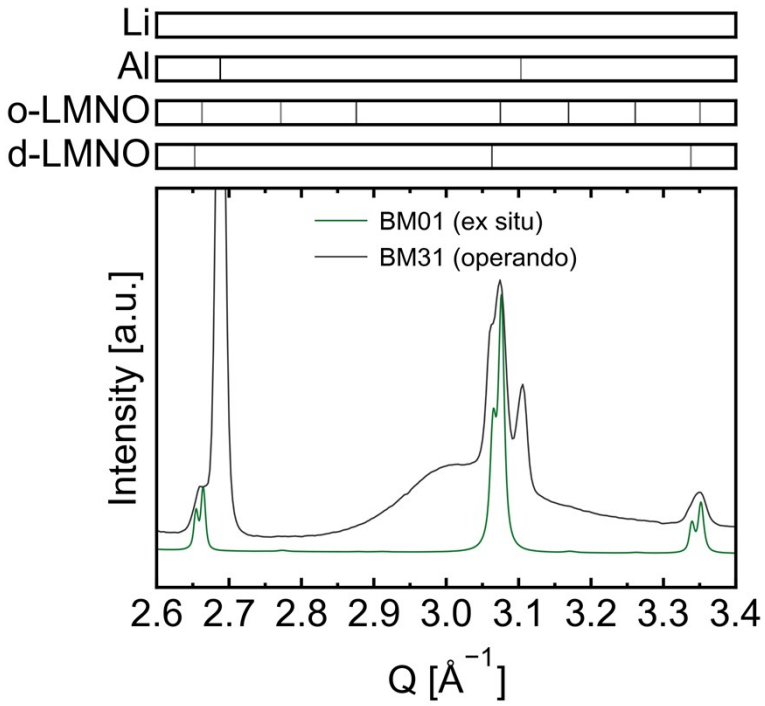

Supporting Figure 31 showing diffractograms of Mn1.6-500C-72h, and the difference from ex situ capillary measurement at BM01 (analogous to the other ex situ samples presented in this work) and operando measurement before experiment started. Even though resolution is much worse in the operando experiment, the peak splitting (o-LMNO and d-LMNO) is visible also here. No o-RS can be seen in either diffractograms, meaning the sample is more or less impurity free.

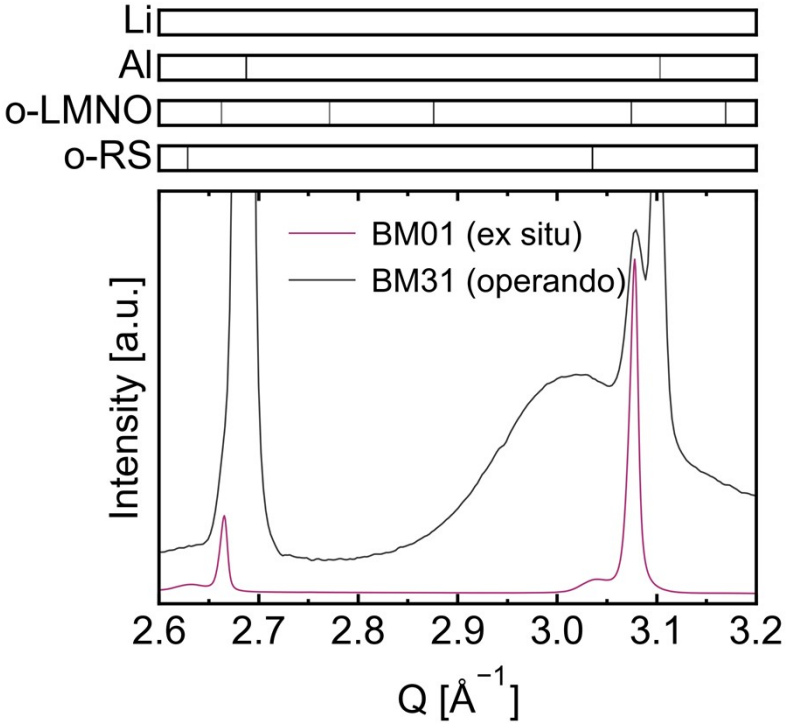

Supporting Figure 32 Similar to Supporting Figure 31, but here with a sample of Mn1.5-stoichiometry (Mn1.5-500C-72h). Here a o-RS phase is present from the ex situ data at BM01, but due to noise this is hardly visible in the operando cell. The (222)-reflection (if any) around Q= 2.625 Å^{-1} in the operando-cell is very difficult to separate from the background signal, whereas the usually most prominent (400)-reflection around Q = 3.04 Å^{-1} is invisible due to drowning in the amorphous signal from the glassy carbon windows of the operando cell.

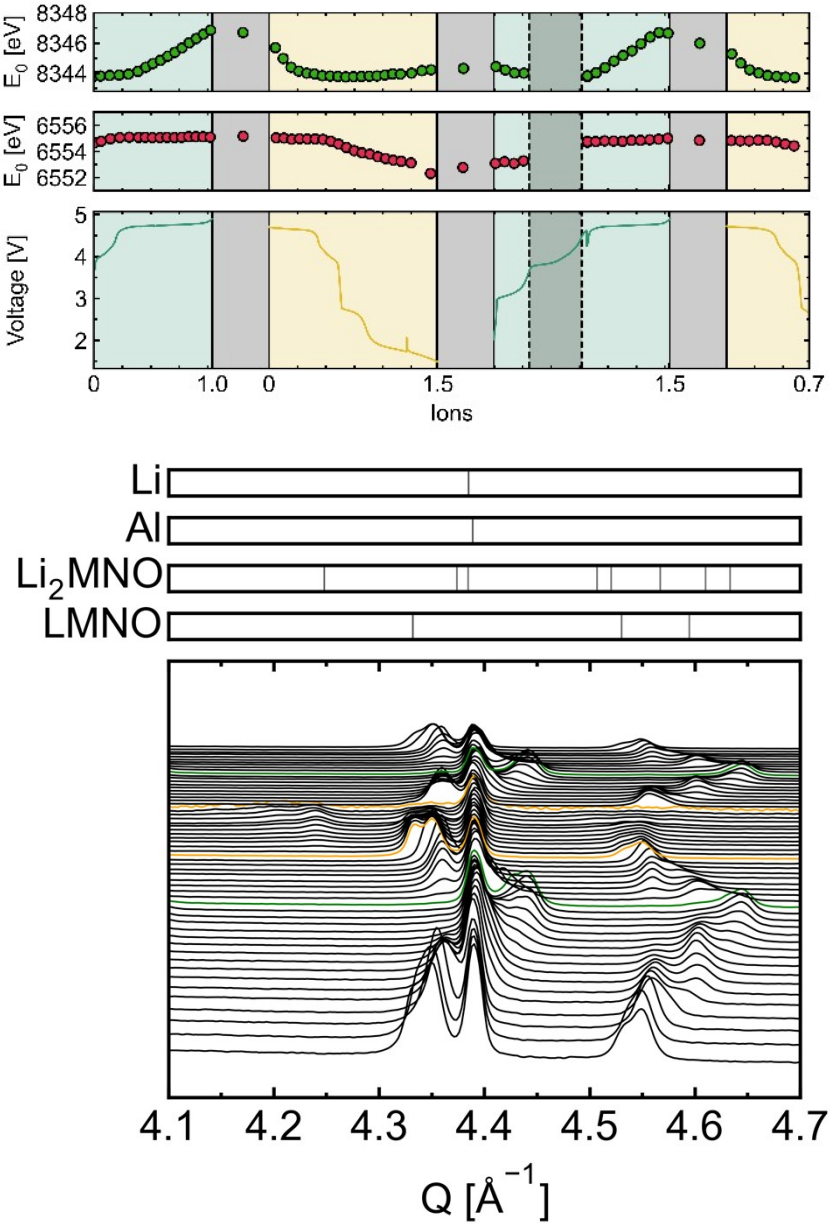

Supporting Figure 33 Overview of operando-experiment on the Mn1.6-500C-72h sample. ***Top panel*** *shows the full experiment with electrochemical cycling data and the analyzed time resolved XANES-spectra; for Mn the pre-edge position is plotted whereas for Ni it is the position of the inflection point.*
The ***bottom panel*** *shows all (usable) diffractograms – from the first (bottom) to the last (top). The green diffractograms represents the fully charged state, whereas the orange lines represent the beginning and the end of the low voltage discharge, as showcased in Figure 14c.*
Experimental information: *It is worth to notice that there were problems with the instrument building up over time, which was not detected right away – leading to the battery continuing to cycle for some time without any meaningful data being collected. For the XANES-data (transmission), that means that data collected in the shadowed region marked with dashed lines in the top panel was not analyzed, whereas for the diffraction this led to data not suitable for Rietveld refining already at the end of the first discharge. This is why the diffractogram measured at 1.5 V is not included in Figure 14d, and colored pink in Figure 14c – and why no data is given for the low-voltage charging region. In the bottom panel all diffractograms after the upper orange line is thus removed until the instrument was fixed, and the cell was restarted around 4.5 V.*
Refinement details: *Several broad peaks were added to account for the amorphous elements in the cell (especially glassy carbon windows), as well as the inactive Al (refined) and Li (LeBail) peaks throughout. For LMNO, L2MNO and L2.5MNO most parameters were kept constant – except a 8 degree polynomial describing the background, in addition to lattice parameters and mass fractions of the four relevant phases. If no meaningful fit was obtained (due to too small/broad peaks) the phase was excluded from the refinement. Lattice parameters remained very stable throughout the refinement series whereas the scale factor/mass fraction was varying a lot (as seen in Figure 14d in the article). Beq-values and occupation numbers of tetragonal phases were locked to that found by Jobst et al (ref 57 in article).*

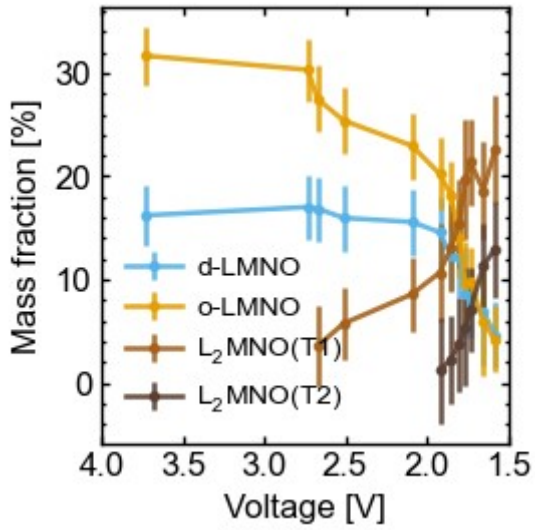

Supporting Figure 34 Same as Figure 14d) in the manuscript, only showcasing error bars representing the errors in the refinement, as reported throughout the manuscript.

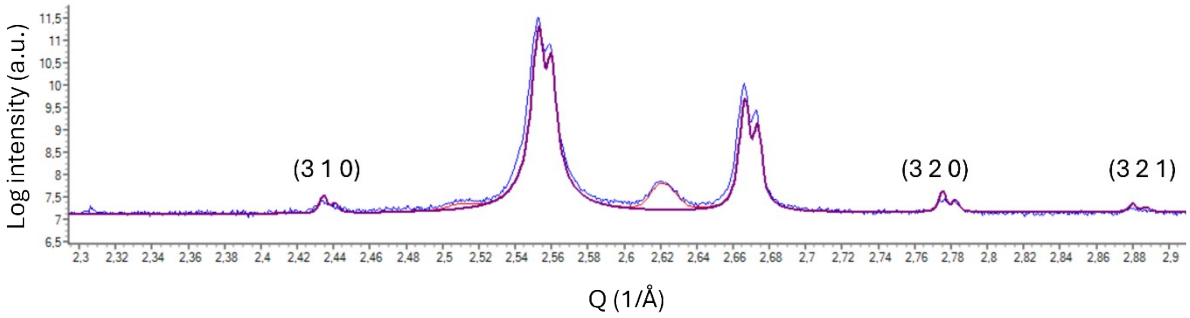

Supporting Figure 35 Supporting Figure 35 Diffractogram of a sample similar to Mn1.5-MO measured in the home lab, showing the ordering peaks (310), (320) and (321). ***Experimental details:*** *Finely crushed powder was dispersed in isopropanol and further ground using an agate mortar and pestle to form a thick slurry. This slurry was drop-cast onto a low-background silicon crystal sample holder and allowed to air dry. Care was taken to ensure the sample surface was flat to minimize errors due to sample height. Data were collected using a Bruker D8 Advance diffractometer in Bragg-Brentano geometry, utilizing a rotating anode Cu radiation source and an XE-T detector with energy filtering technique for fluorescence suppression. The X-ray tube was operated at 45 kV 120 mA without a monochromator. Data acquisition covered a 2ϑ range of 5° to 90°, with a step size of 0.01° and a dwell time of 0.3 seconds per step. The sample holder was continuously rotated during PXRD data acquisition to improve particle statistics and minimize preferred orientation effects.*